D3.6
Signal processing and imaging algorithm extension and optimisation

General information	
Grant agreement number	755500
Start date of the project	01/09/2017
Project duration	48 months
Due date of the deliverable	31/12/2019
Actual submission date	18/08/2020
Lead beneficiary	KTU

Keywords
TRL transducers

Type	Meaning	
R	Document, report	x
DEM	Demonstrator, pilot, prototype	
DEC	Websites, patent fillings, videos, etc.	
OTHER	Software, technical diagram, etc.	

Dissemination Level		
PU	Public	x
CO	Confidential, only for members of the consortium (including the Commission Services)	

Table of Contents

Table of Tables

Table of Figures

 © ADVISE consortium

1 Executive Summary

TRL (for transmit-receive-longitudinal) transducers, also known as SEL transducers, are the method of choice for the inspection of coarse grain cast (or forged) austenitic stainless steel. These transducers use separate transmit and receive elements in a single housing and generate refracted longitudinal waves. Employing both an angle in the incidence plane and a roof angle, TRL transducers reduce the effective material volume generating backscatter that actually makes it back to the receiver. Two wedge angles determine the distance where two sound fields of transmission and reception overlap. The separation of transmitter and receiver also avoids the otherwise existing blind zone, allowing the detection of defects close to the surface. The concept requires an acoustic separation of the two transducers. TRL transducers were introduced in the early 1990s as two-crystal transducers with refracted angles of 55° for standard applications and 70° for inspection close to the surface. Today, TRL transducers are also available as linear or asymmetrical matrix array (with limited roof steering capability), to cover different depth ranges with a single transducer.

Being the reference method for the inspection of coarse grain materials, it is essential that advanced imaging algorithms developed in the ADVISE project be not only compared to standard TFM (using 0° matrix arrays), but to two element TRL transducers. With the advent of phased array TRL transducers, however, the project should also evaluate the potential advantages of combining TRL with advanced imaging methods, in particular those derived from TFM. In case of TRL set-up an improved S/N ratio is expected compared to standard TFM, as all receiving elements should provide a useful contribution to the imaging algorithm as opposed to the 0° TFM, where the elements close to the transmitting element are likely to suffer from backscatter noise.

This report has two primary aims: 1) to evaluate the performance of TRL array probes with the arrays used in 0° TFM and 2) to investigate the efficiency of Super Resolution (SR) and phase-coherence TFM methods applied for TRL inspection of heterogenous nuclear materials. It has been shown by different studies that for noise-free materials, the TFM with the phase coherence correction gains some super-resolution features, while for grained materials it has been shown to improve the SNR significantly. In this report we intend to apply phase coherence TFM to TRL set-ups and to evaluate the SNR improvement over 0° TFM and TRL-TFM without phase correction. SR algorithms allow for a refinement of an ultrasonic array image of a small area, with an a priori knowledge of the defect location. They are known to perform poorly in noisy configurations and are typically suitable only when SNR is above 20 dB - a scenario often not available in coarse-grained components. However, it’s expexted, that TRL set-up and low inspection frequencies will reduce the backscatter creating favourable environment for SR methods.

The key findings of the study show, that TRL-TFM enables to improve the SNR by 3-4dB on average in comparison to 0° TFM. It was found that SR algorithms do not provide a reliable way to compute array images for coarsely grained materials, due to the sensitivity to noise, and even the best variant, enhanced by phase coherence was not able to recover defect signatures from the noise level to a satisfactory degree. On the other hand, phase coherence TFM demonstrated improvement in both SNR and CNR significantly, often well over 20 dB, increasing the resolution at the same time. They were found to be more robust to structural noise and were found considerably clearer than the corresponding SR images. In general TRL-TFM set-ups showed more inspection flexibility compared to classical approaches. The custom 0° incidence TRL wedges that have only roof angle were investigated. The observations can be made that 0° incidence TRL wedges with matrix arrays allow to dynamically steer the roof angle and change the beam convergence depth. Additionally, both linear and matrix arrays can be used with 0° incidence TRL wedges to steer the beam in frontal direction, achieving different incidence angles. As a result, one wedge could be used instead of a set of wedges for longitudinal wave focusing at particular depth and incidence angle.

 © ADVISE consortium

2 TRL phased array imaging

The objective of this section is to evaluate the ability of TRL array probes to detect and image defects in heterogeneous nuclear materials and to compare their performances with those of arrays used in pulse-echo (PE) mode. To do this, a series of experiments were carried out with a sample of static cast stainless steel supplied by EDF and Framatome, using a pair of matrix and linear arrays.

2.1 Mock-ups and probes

This section describes sample mock-ups and probes used for TRL task. The mock-ups for TRL imaging experiment were provided by EDF and Framatome. The sample provided by EDF is a 100×480×91 mm^3 static cast stainless steel (**D343-CND2**) mock-up with columnar and equiaxed grain structure. It has 10 side drilled holes of 2mm diameter machined at different depths (Figure 1a). The metallographic photo (Figure 1b) clearly reveals two layers of different microstructures: the upper layer is composed of equiaxed grains (isotropic layer), while the lower layer is formed of columnar grains (anisotropic layer). The 4 deepest artificial defects are located in the anisotropic layer, and the 5 shallower ones in the isotropic layer (1 flaw is located at the junction between the two layers). Throughout the study, for real-time imaging or reconstructions by post-processing experimental data in the CIVA software, the phase velocity of the L waves was assumed to be constant and equal to 5650 m/s. This rough approximation may explain some problems of positioning of the defect echoes in the images that was obtained and discussed in the upcoming sections. The exact defect positions are of the (**D343-CND2**) mock-up summarized in Table 1.

The Framatome mock-up (**RDIM3**) is a segment of a pipe with radius of 400 mm. It has a coarse grained homogenous structure of 18% fine grain (average grain index 0.5, diameter = 0.3mm) in a matrix of 82% coarse grain (average grain index -5.5, diameter = 2.4mm). Five flat bottom holes of 3mm diameter are located at different depths as target defects in this mock-up as it can be seen in Figure 2a. The exact defect positions are summarized in Table 2.

Table 1**:** Defect positions at sample D343-CND2

Defect reference	T5	T10	T15	T20	T30	T40	T50	T60	T70	T80
Ligament (mm)	5.2	10	15	20.1	30.2	39.8	50.1	61.5	70.2	81.2
Offset from left egde (mm)	20	40	65	90	140	200	280	325	370	410

Table 2: Defect positions at sample RDIM3

Defect reference	A	B	C	D	E
Ligament (mm)	10	20	40	60	80
Offset from left egde (mm)	60	120	180	240	338

© ADVISE consortium

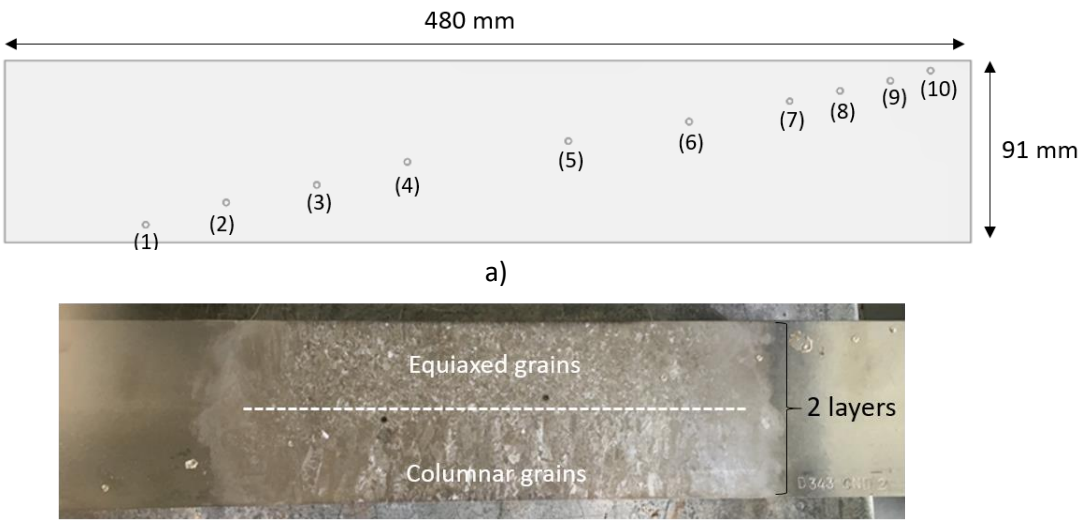

Figure 1: Block of static cast stainless steel (D343-CND2) supplied by EDF for the TRL measurements: geometry of the sample and location of 10 side-drilled holes in the thickness (a); metallographic view emphasizing two layers with different microstructures (b).

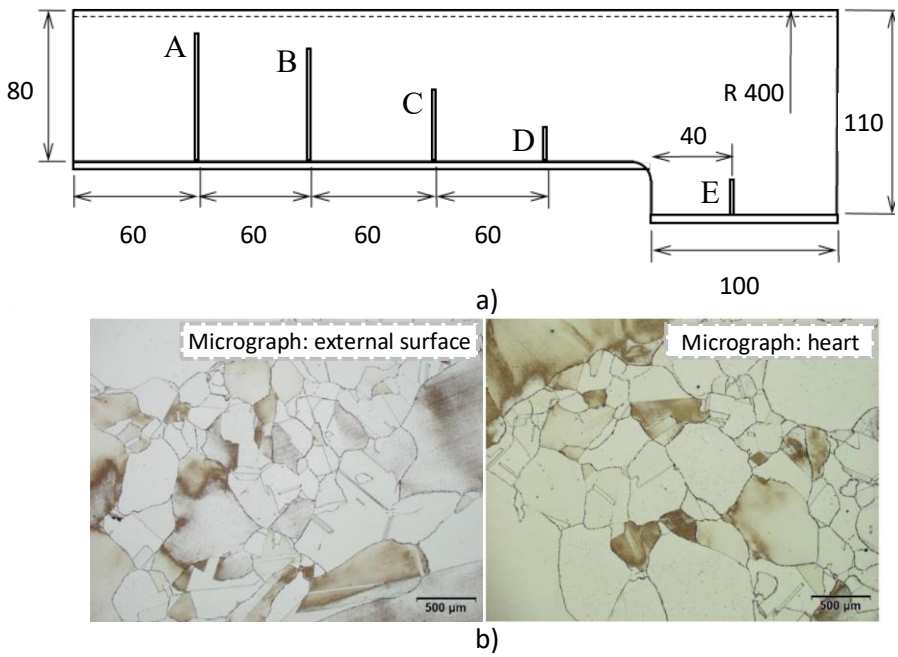

Figure 2: The schematic diagram of the mock-up RDIM3: geometry and locations of the FBH defects (a); micrographs representing grain structure in heart and surface of the component in the plane of imaging (b)

The TRL task was performed using two distinct set-ups:

- CEA has done the measurements on the flat mock-up (**D343-CND2**) provided by EDF using a pair of matrix arrays (Imasonic, France).
- KTU did the acquisitions on sample (**RDIM3**) provided by Framatome using linear phased array approach (Imasonic, France).

2.1.1 Description of matrix TRL arrays and wedges

A pair of 2 MHz (80 % bandwidth at – 6 dB) 16×4 matrix arrays were selected by CEA for measurements on sample **D343-CND2**. Each probe is composed of 16x4 piezoelectric elements: 16 elements in the incident plane with a pitch of 2.8 mm, and 4 elements in the orthogonal plane with a pitch of 5.05 mm. The active surface of an element is 2.6×4.85 mm², where 4.85 mm is the element width in the orthogonal plane. The

whole active aperture of a matrix is therefore 44.6×20 mm² with an aperture more than twice as large in the incident plane. The photo displayed in Figure 3 shows the pair of matrix arrays, as well as a set of 3 wedges for focusing longitudinal (L) waves at different angles and depths used by CEA. The first is designed to focus waves around an angle of refraction of 60° and at a depth of 10 mm. It was not selected for our measurements because scattering noise at 2 MHz is not significant at 10 mm in the EDF sample. The other two wedges were more interesting for the present study, since they focus ultrasound at depths of 60 and 30 mm where structural noise becomes significant. Both are designed for focusing refracted beams around 45°. The phase velocity in the wedges is assumed to be 2350 m/s.

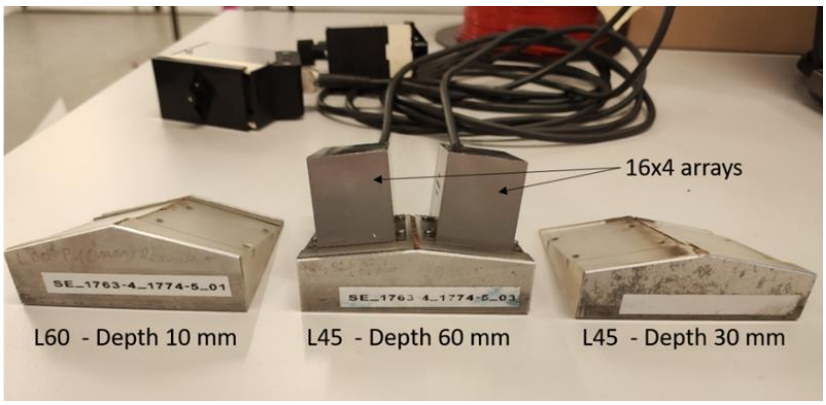

Figure 3: TRL matrix arrays with a set of 3 wedges for focusing with L waves at different angles and depths: 60° and 10 mm (left); 45° and 60 mm (center); 45° and 30 mm (right)

The geometrical characteristics of the two L45 wedges are presented in Figure 4 below (screenshots of the CIVA software). The dimensions and angles of the wedges were accurately measured as a precaution since they can strongly affect the quality of images.

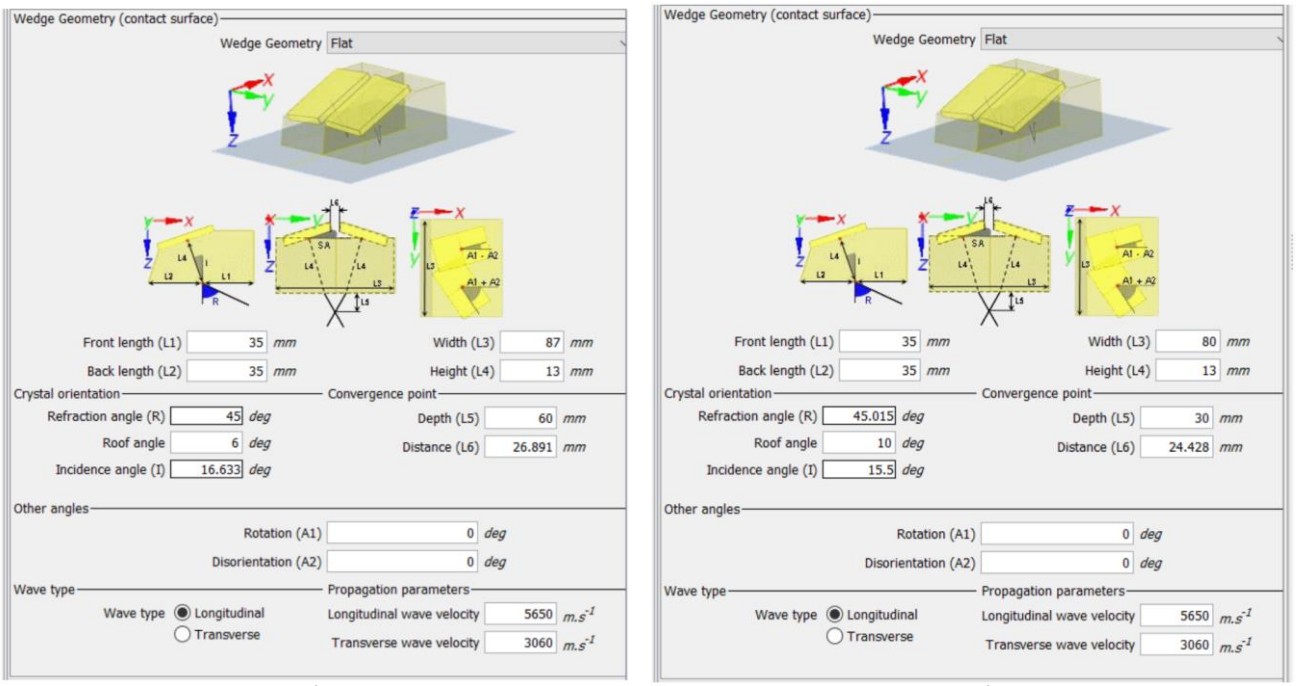

a) b)

Figure 4: Geometries of the two L45 wedges used in the experiments conducted at CEA: wedges for focusing around 60 mm (a) and 30 mm (b)

2.1.2 Description of linear TRL arrays and wedges

For the linear phased array inspection, 1MHz 32 element phased arrays were selected, taking into account the grain structure of the mock-up. The selected array has elements with dimensions of 1.55 mm and 0.5 mm inter-element spacing. As the mock-up (**RDIM3**) has convex surface and FBH type defects, classical commercially available wedges cannot be used for the inspection. In case of FBH type defects, the reflecting surface is in the horizontal plane, hence the reflection from it cannot be obtained using incident excitation. Theoretically, edge waves can be produced from tip of FBH in case of incident excitation, but the acquisition of such signals taking into the account structural noise of the component is impractical. In case of FBH assessment, the sound field which is reflected from the tip of the defect propagates back to the transducer on the sample plane. Therefore wedges with 0° incidence are required to be able to record the reflected signals. For this purpose, special 0° incidence wedges were manufactured which have a roof angle only to interrogate with the structure at certain depths. The specially designed wedges are illustrated in Figure 5. It should be noted that the diameter of the FBHs is equal to 3mm, which makes them challenging to detect in coarse grained materials as their size is equal to half a wavelength at 1MHz in stainless steel. On the other hand it is expected that the benefits of TRL such as reduced effective volume that generates backscattered noise may provide an improved reconstruction even for such small defects.

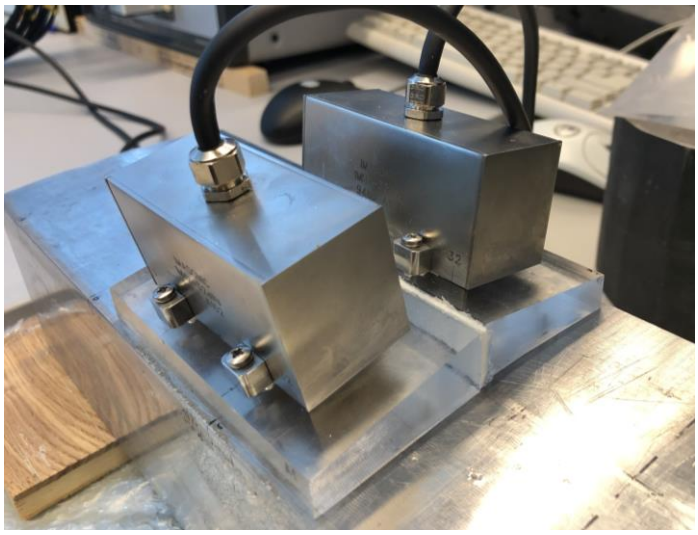

Figure 5: The 0° incidence angle wedge for inspection of convex samples with FBH

The wedges for FBH inspection were designed with a roof angle of 10° which theoretically ensures the focal point at 50 mm depth. The presumed velocities at the plexiglass wedge were 2700 m/s and 5900 m/s at steel. An extruded polystyrene foam was inserted as an acoustic separator. The exact dimensions and crystal orientations for the designed wedges are presented in Figure 6a. As it can be observed from Figure 6a, the actual convergence point for the FBH TRL wedge is at a depth of 62.6 mm, which is increased from theoretical estimation due to its concave surface. Additionally, the sound field in stainless steel for the 0° incidence wedge was calculated using CIVA and presented in Figure 6b. The soundfield length at –6dB level is 40mm (starting at depth of 40mm and ending at 80mm for stainless steel). As a result, it is expected to be able to assess C, D and E FBH's using 0° incidence angle wedge for sample **RDIM3**.

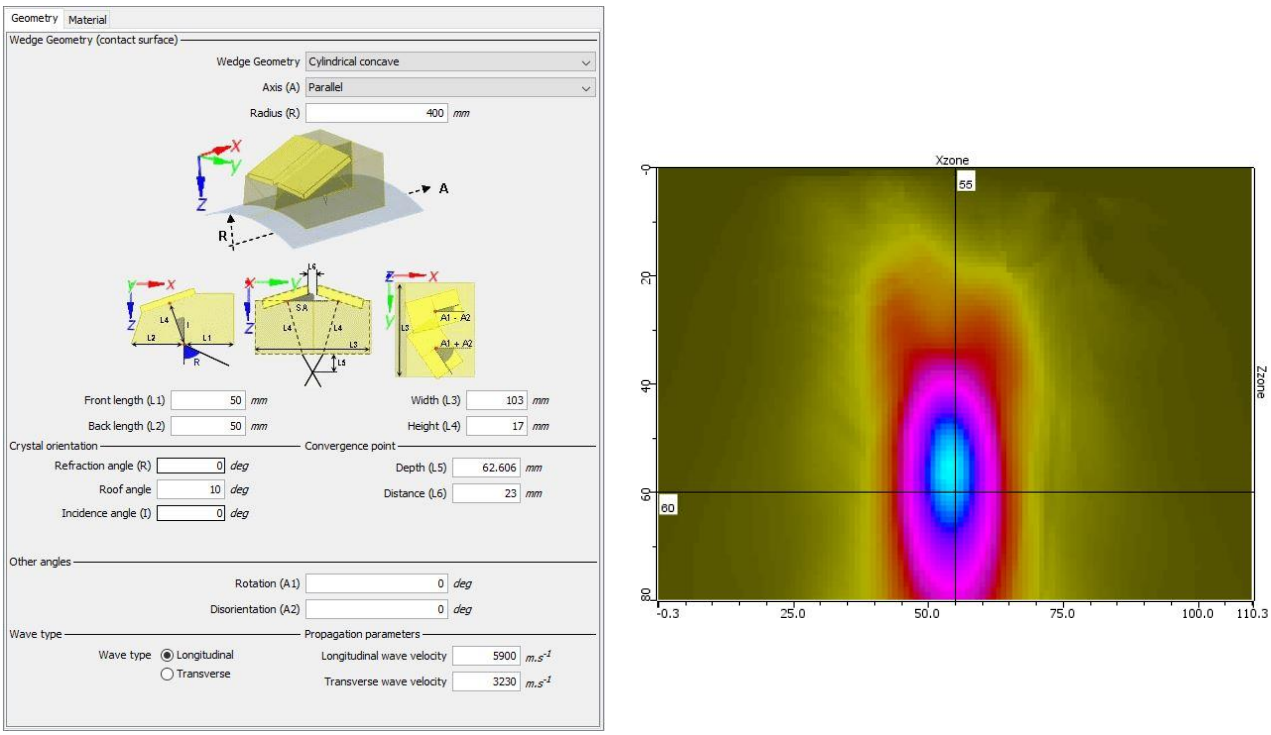

a) b)

Figure 6: The dimensions and crystal orientations of wedge for FBH inspection with convex surface (a) and the sound field in stainless steel for 1 MHz 32 element phased array with cylindrical concave wedge geometry possessing 0° incidence angle and 10° roof angle (b)

2.2 Matrix TRL phased array imaging

This section presents imaging results using matrix TRL arrays available at CEA. Experimental data were collected with a multichannel Eddyfi system, and images were computed by post-processing in the CIVA software. Three imaging methods were evaluated and compared with each other: focused SScan, Total Focusing Method (TFM) and Plane Wave Imaging (PWI). In the following, we first describe the experimental set-up. Then, we present and analyze the images of side-drilled holes (SScan, TFM, PWI) obtained with the TRL matrix arrays. Finally, we compare the images obtained with the TRL and PE inspection configurations, and give some results of 3D beam computation with CIVA to interpret the results.

2.2.1 Experimental set-up

Two photos of the experimental bench are shown in Figures 7a and 7b. A wire encoder system was used to accurately position the probe at a distance from a given defect. The current position and the corresponding ultrasonic data were recorded with a 256 multi-channel MultiX system (Eddyfi Technologies).

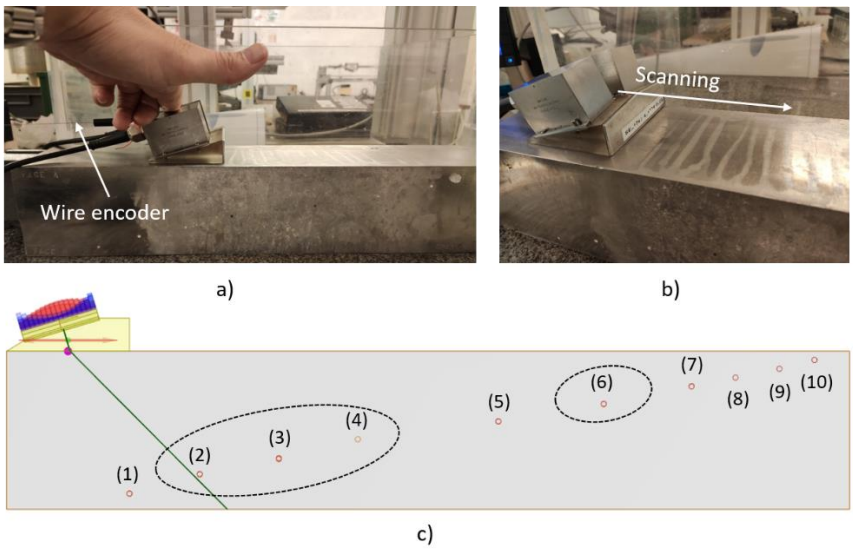

Figure 7: Photos of the experimental bench with a wire encoder system to measure the probe positions (a) and view of the TRL matrix arrays associated with a linear scanning (b). CAD view from the CIVA software with the SDH locations: the FMC data are recorded in 4 positions to image SDHs (2), (3), (4) and (6)

The CAD view in Figure 7c shows the location of the 4 defects for which we recorded the FMC data: SDHs (2), (3) and (4) with wedge no. 1 (focal depth of 60 mm) and SDH (6) with wedge no. 2 (focal depth of 30 mm). SDH (1) is not detectable because it is too close to the left edge of the sample, while wedge no. 2 is not suitable for imaging SDHs (5), (7), (8), (9) and (10) since they are too far from the focal depth of 30 mm. For each defect, Table 3 gives the type of L45 wedge used to collect the FMC data, as well as the X position of the TRL probe. The values of X indicated in the table correspond to the distances from the left edge of the sample to the wedge center. As shown in Figure 8, the positions were chosen so that the central ray of the plane wave refracted with an angle of 45° passes through the defect center. This is because the propagation direction of a plane wave generated with a null delay law can be interpreted as the main direction of energy for a FMC acquisition.

Table 3: DHs selected to evaluate the TRL matrix arrays: depths of the 4 SDHs, focal depths of the L45 wedges, X positions from the left edge of the sample to record the FMC data.

SDH	2	3	4	6
Depth (mm)	70	60	50	30
Focal depth of the *L45* wedge (mm)	60	60	60	30
X position for imaging (mm)	40	94	150	310

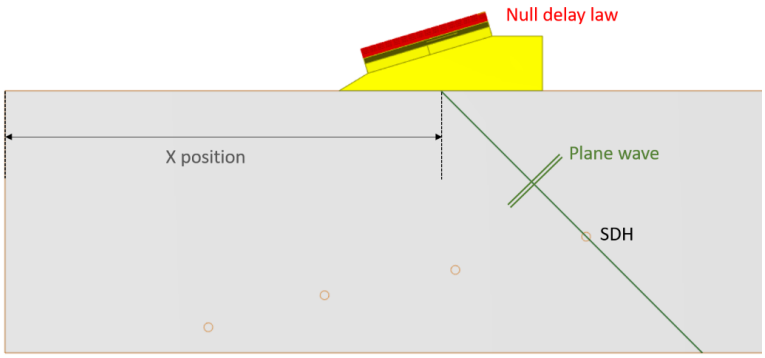

Figure 8: Positioning method for the FMC acquisitions with a L45 wedge: the TRL probe is positioned so that the central ray of the 45° refracted plane wave crosses the defect

© ADVISE consortium

2.2.2 TFM images

The FMC data were recorded with a sampling frequency of 50 MHz, and using a single matrix of 16×4 elements as the transmission array, as described in Figure 9. The second matrix is the reception array that records the 64 signals at each transmission sequence. Thus, the FMC acquisition file consists of 64^2 signals. It should be noted that a second set of 64^2 signals can be recorded using the second matrix as the transmission array, but the signals would not provide more information due to the reciprocity principle. Furthermore, the other 128 pulse-echo signals recorded with elements used as both transmitter and receiver are not relevant for imaging with a TRL inspection configuration, and may affect the image quality because of the emergence of wedge echoes. Thus, the 64 signals recorded according to the principle shown in Figure 9 are the most relevant data for imaging.

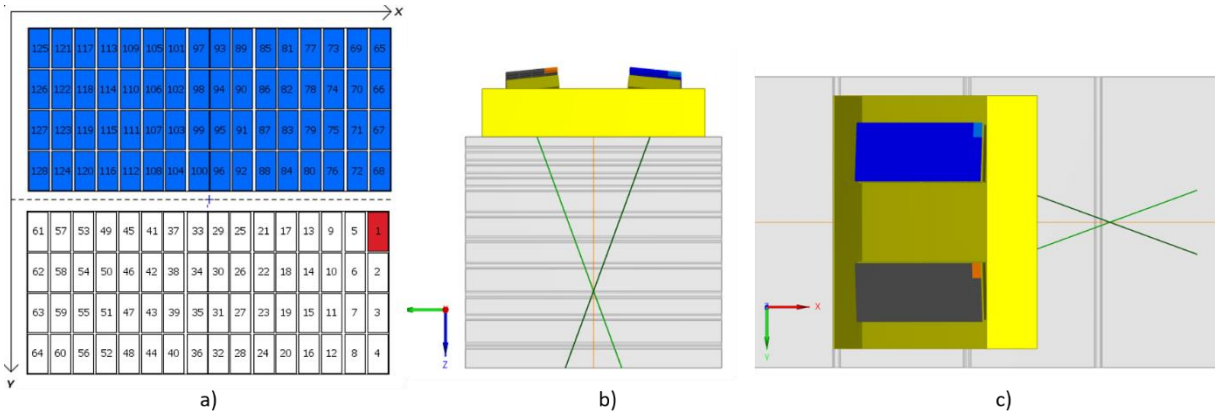

Figure 9: Full Matrix Capture for the TRL matrix arrays: a single matrix is used as 16×4 transmitter array and the second matrix records 64 signals for each transmission with 1 element (a); screenshots of the CIVA software with the side view (b) and top view (c) of the TRL matrix arrays

The TFM images of the 4 SDHs are displayed in Figure 10, and can be compared with the SScan images obtained with a sectorial scanning between 25 and 65°(angular step of 1°) and by focusing at the depth of the corresponding defect. We observe that the image quality is surprisingly good at a frequency of 2 MHz, even for the deepest reflector at 70 mm. The SNR increases from 9 to 20 dB for depths ranging from 70 to 30 mm. The SNR evolution follows a similar trend for the SScan images, except that the SNR is 3 dB lower on average. This slight difference of SNR is due to the high-pass filter applied to the FMC data to obtain zero-mean signals before imaging (rectangular filter removing the spectral content below 0.5 MHz). The same filter could not be applied for the SScan images because the 64 elementary signals were delayed and summed in the system hardware before the acquisition step.

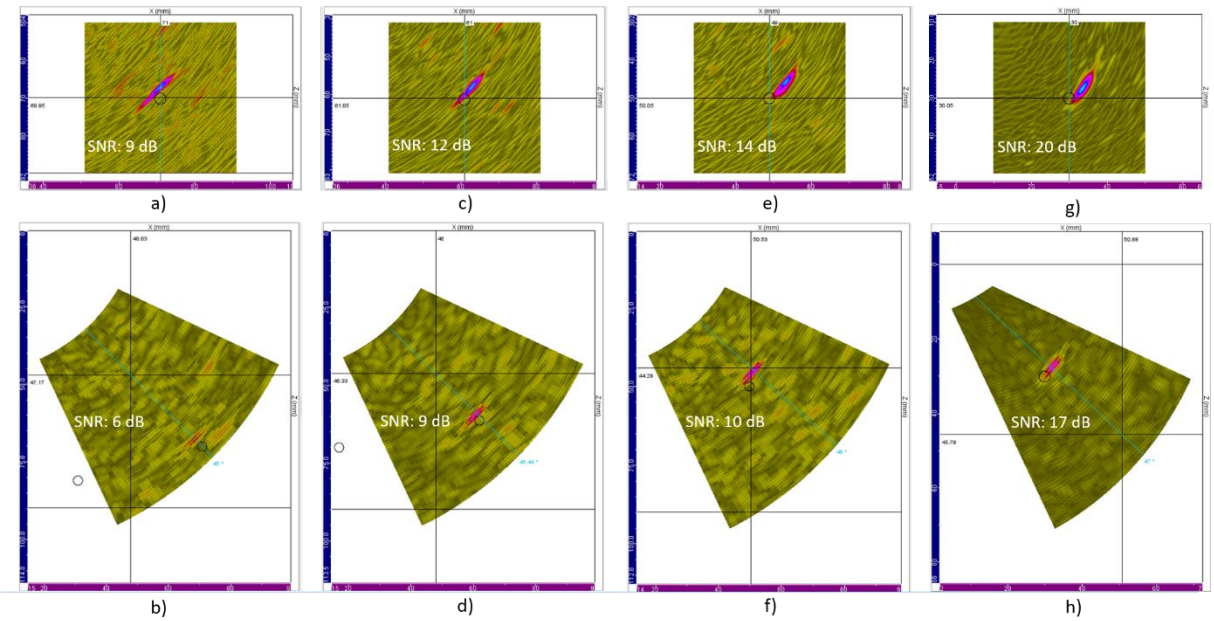

Figure 10: Comparison of the TFM and SScan images for SDHs at different depths: SDH (2) at 70 mm (a)-(b); SDH (3) at 60 mm (c)-(d); SDH (4) at 50 mm (e)-(f); SDH (6) at 30 mm (g)-(h)

The second observation is a slight discrepancy between the positions of the echoes and the actual positions of the defects (represented by circles in Figure 10). The positioning error tends to increase when the depth decreases, which is probably due to a variation in phase velocity with depth. As described previously, the upper layer is composed of equiaxed grains and should be almost isotropic, while the lower layer formed of columnar grains should be anisotropic. Thus, L waves propagating around 45° should have slightly different velocities in the two layers.

2.2.3 PWI imaging

To further improve the SNR of images, acquisitions with plane wave emissions were carried out using the same experimental set-up and multi-channel system. The CIVA software is able to compute PWI images from data recorded with any type of probe and wedge. In Figure 11, an experimental PWI image formed with the TRL matrix arrays is displayed in different CAD views of the software, as well as the ray tracing associated with plane wave emissions (each ray is the central ray of a plane wave). As for the FMC acquisition, one matrix (in red) is used as the transmission array, while the second one (in blue) records the 16×4 signals for each plane wave emission. To form PWI images with a spatial resolution similar to that of the TFM images, each defect was insonified by 31 plane waves in a wide angular range (between 30 to 60° with the angular step of 1°). It should be pointed out that plane waves are not deflected in the orthogonal plane of the transmission matrix. This means that the propagation directions of plane waves are not ideally suited for imaging a defect whose depth does not correspond to the focusing depth of the TRL wedge (60 mm for wedge no. 1 or 30 mm for wedge no. 2). The results could be slightly improved for SDHs (2) and (4) with a deflection of the plane waves in the orthogonal plane to adapt to the inspection depth.

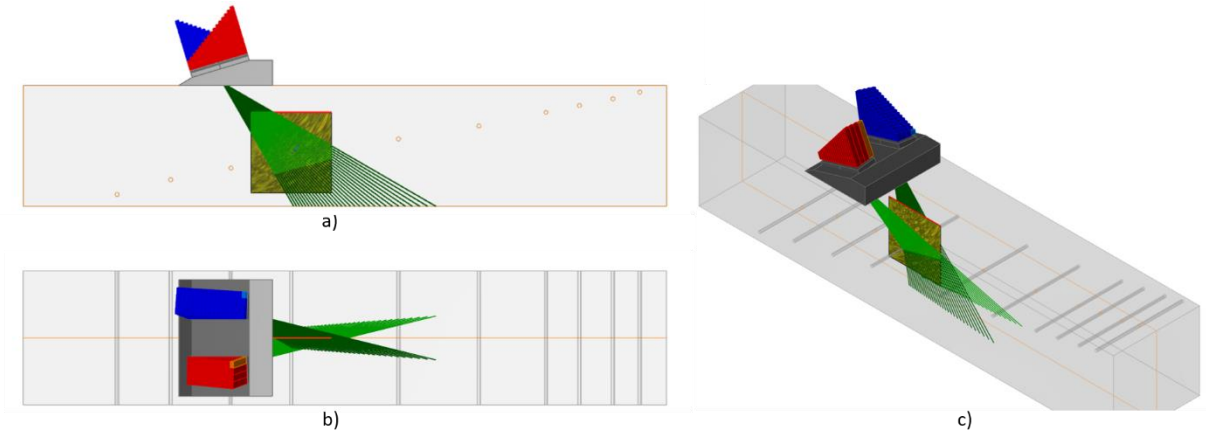

Figure 11: Experimental PWI image computed in CIVA: front view (a); top view (b); perspective view (c).

The PWI method was evaluated only with wedge no. 1 for which the values of SNR obtained with TFM are lower than 14 dB. The images of SDHs (2), (3) and (4) are presented in Figure 12, and can be compared with the TFM images. For the two imaging methods, the same discrepancies between the positions of the echoes and the actual positions of the SDHs are observed. As expected, the main difference between PWI and TFM is a better SNR for PWI. The SNR is increased by 4 dB on average, while the number of transmissions is reduced by a factor of 2. This is a well-known result in heterogeneous materials: diverging waves are more attenuated than plane waves due to the cylindrical spreading and the inverse distance law, and, since diverging waves interact with a maximum number of heterogeneities, they tend to increase the scattering noise contribution. A plane wave interacts with fewer heterogeneities of the material because the illuminated region is limited by the array aperture, and thus the scattering noise contribution is reduced.

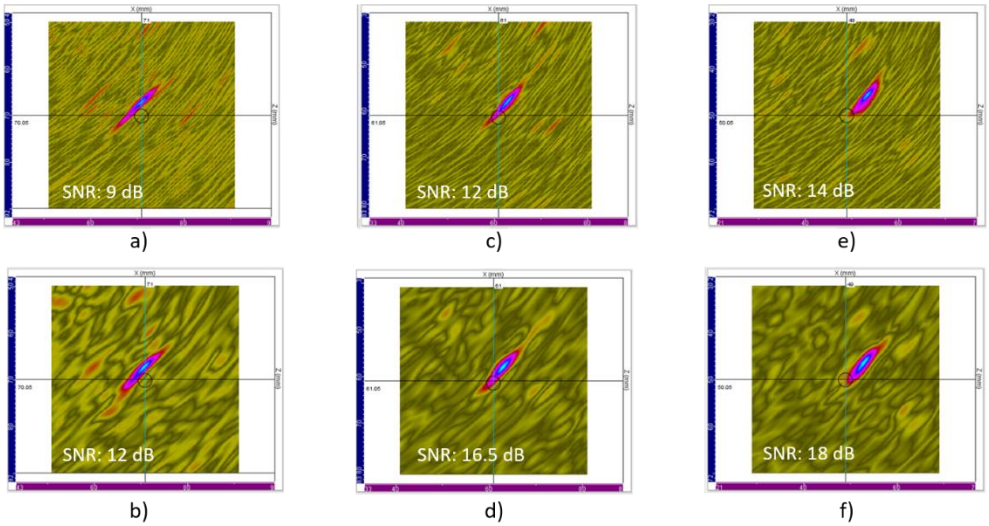

Figure 12: Comparison of the PWI and TFM images for SDHs at different depths: SDH (2) at 70 mm (a)-(b); SDH (3) at 60 mm (c)-(d); SDH (4) at 50 mm (e)-(f)

2.2.4 Comparison of TFM images obtained in TRL mode and in PE mode

Another experiment was conducted to demonstrate the advantage of TRL probes over arrays used in pulse-echo (PE) mode for imaging in heterogeneous materials. One of the two matrix arrays was placed directly (without wedge) on the EDF sample to image SDHs (2), (3) and (4) in PE mode with TFM. The matrix array was centered on each defect (L0 inspection), and FMC data were recorded using the same acquisition settings as in TRL mode: excitation voltage 70 V, pre-amplification gain 70 dB, sampling frequency 50 MHz. In

addition, the same high-pass filter (rectangular filter removing the spectral content below 0.5 MHz) was used for both PE and TRL mode acquisitions. The results are shown in Figure 13, and we can notice that the echoes of the 3 defects are well positioned for the L0 inspection configuration. It can be assumed that the phase velocities in the two layers are almost identical in the vertical direction, which is not the case for the 45° incidence inspection. As far as SNR is concerned, it is slightly higher for images obtained with the TRL configuration, except for SDH (4) where the images are of equivalent quality.

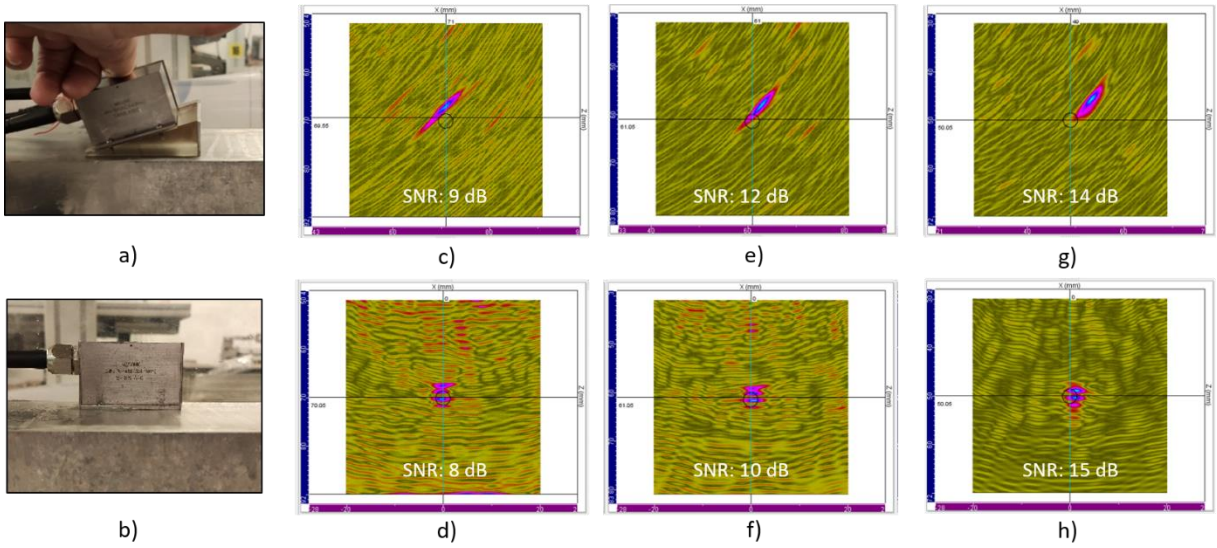

Figure 13: Comparison of the TFM images obtained in TRL mode (a) and in PE mode (b) for SDHs at different depths: SDH (2) at 70 mm (c)-(d); SDH (3) at 60 mm (e)-(f); SDH (4) at 50 mm (g)-(h)

To interpret the above SNR differences, the focused 3D beams generated by the TRL and PE matrix arrays were computed with the CIVA software (see Figure 14). In both cases, the focal point is located on SDH (3) at the depth of 60 mm, and the beam was computed in transmit/receive mode assuming an isotropic and homogeneous steel sample (constant phase velocity of 5.65 mm/µs) and without taking into account attenuation. Figure 14 also displays the 3 orthogonal sections for each 3D beam. We see that the lateral resolution is almost twice better for the array used in PE mode: the width of the focused beam is 4.8 mm in the incidence plane for the TRL matrix arrays, and 2.5 mm for the matrix array used in PE mode. Another relevant information supplied by the beam computations is that the amplitude at the focal point is 5 dB lower for the beam generated by the pair of TRL matrix arrays. Including attenuation, the amplitude difference would be even greater because the wave paths are longer with a TRL configuration. Thus, simulations without scattering noise show that focusing with a PE probe is more efficient in terms of detection amplitude compared to TRL probes, while experimental results show similar or even better results with TRL probes. From this analysis, we can conclude that the efficiency of TRL probes for imaging in heterogeneous materials lies in the separation of the transmission and reception apertures, which decreases the noise correlation between the forward and backward wave paths.

 © ADVISE consortium

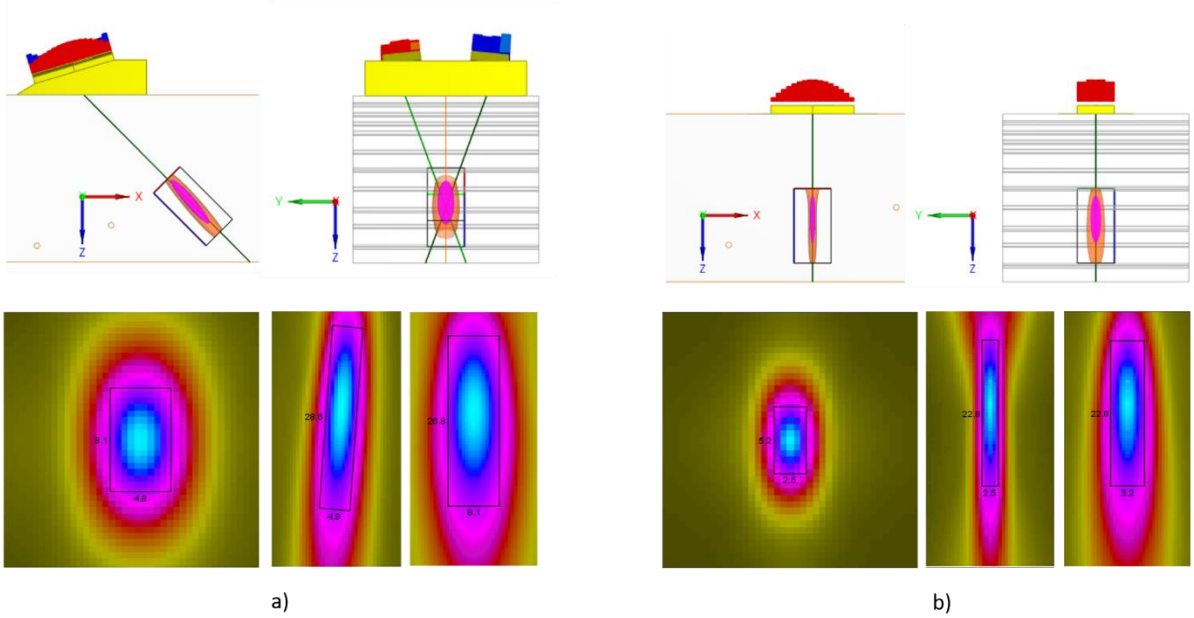

a) b)

Figure 14: Computation of 3D beams focused at the depth of 60 mm: (a) beam generated by the pair of TRL matrix arrays and orthogonal sections extracted at the focal point; (b) beam for the matrix array used in PE mode and orthogonal sections extracted at the focal point

2.3 Linear TRL phased array imaging

This section presents imaging results using linear TRL arrays available at KTU. This chapter is organised as follows:

- The FBH inspection CIVA modelling is presented in order to obtain expected reflection magnitudes in case of assessment of FBH defects.
- The general algorithm for TFM reconstruction is described, which will be used in throughtout this section.
- The extension of classical TFM to the case of 0° incidence TRL with two media is discussed, followed by verification of the approach and reconstruction results from the Framatome sample.
- Later, the TFM extension to samples with convex surface is discussed and presented.
- The experiments with 0° TFM are performed to obtain reference data, which is later used in comparison with TRL reconstruction.
- Finally, the sample curvature and conventional TRL reconstructions are illustrated with some examples.

2.3.1 FBH inspection modelling

The aim of this section is to create a model of a pipe segment that correspond to mock-up **RDIM3** and to assess the magnitude of the reflection from FBH at different depths. For the scope of this study the FBH inspection using 0° incidence TRL wedge and 1MHz 32 element linear phased array was simulated using CIVA. The model corresponding to the actual mock-up was created with 4 FBH's (A, B, C and D, see Table 2 for defect reference), each having a diameter of 3mm. The 0° incidence TRL transducer was scanned along the defects to obtain the B-scan image of the sample. The data was acquired in the full matrix capture mode where in each sequence, single element of the transmitting array was fired, while the receiving array was capturing the signals will all elements at once. As a result, the FMC array consists of 32^2 signals. The view of the model and B-scan image can be seen in Figure 15. As it can be observed from the results presented below, the FBH is a weak reflector which produces the magnitude of –33dB to –36dB in respect to the backwall reflection, depending on the inspection depth. At fixed inspection depth, reflection magnitude is a function of excitation frequency, which for the FBH defect D can be expected as presented in Figure 16. As in this case

the excitation frequency of 1MHz is used throughout the experiments, its expected that the reflection magnitude will be approx. –32dB in respect to backwall. At the frequencies above 2MHz, the magnitude curve starts to settle, meaning that 3mm FBH starts acting as a flat reflector. Note, that the coarse grained structure of the sample and backscattered noise was not taken into the account here.

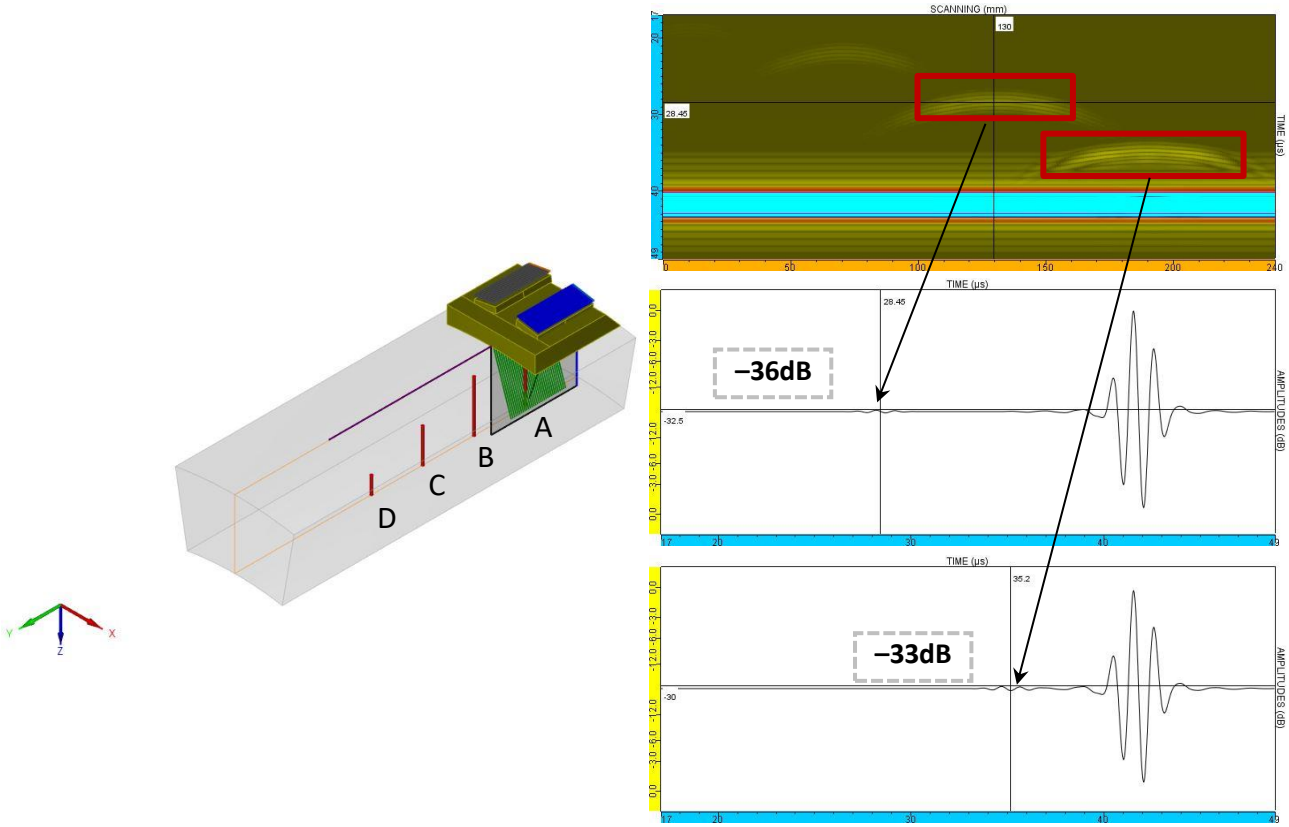

a) b)

Figure 15: The CIVA model representing mock-up (RDIM3) (a) and the B-scan image along the sample indicating the reflections from defects (b)

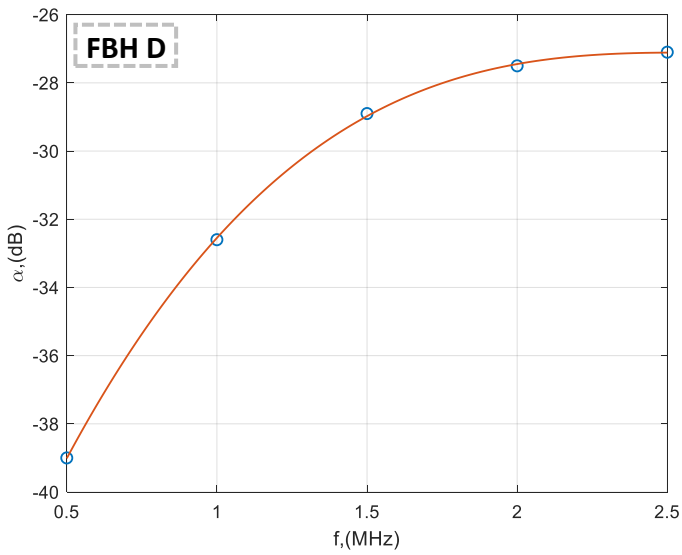

Figure 16: The reflection magnitude from FBH D in respect to back-wall reflection at different excitation frequencies

Additionally, the TFM reconstruction of the simulated FMC signals were performed in CIVA to reconstruct the reflections from holes C and D. The reconstructed defects were selected according to the

sound field convergence point inside the material as for 0° incidence and 10° roof angle wedge, the reconstruction depths are from 40mm to 80mm (see Figure 6 for reference). The TFM reconstruction of the defects is presented in Figure 17.

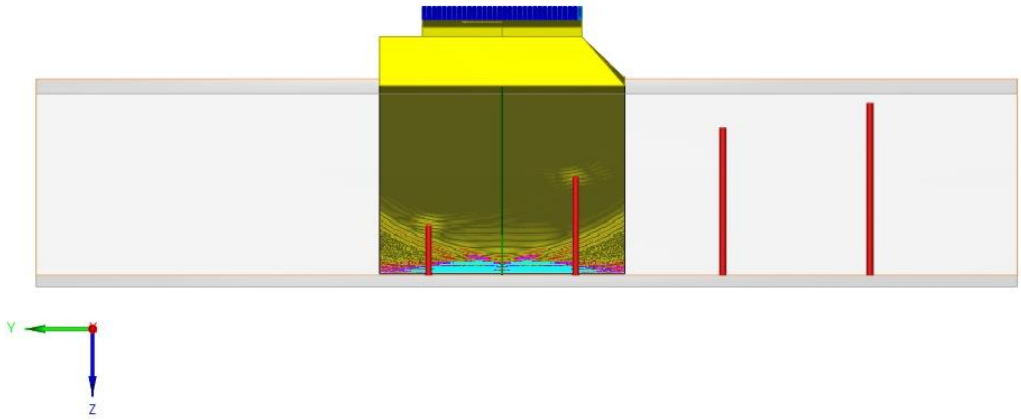

Figure 17: The TFM reconstruction of FBH on convex sample using 0° incidence angle TRL set-up

2.3.2 General algorithm for TFM reconstruction

The 3D space for reconstruction is determined as the set of spatial coordinates $\mathbf{S}_N(\mathbf{X},\mathbf{Y},\mathbf{Z})$, where *N* is the total number of points. As input data are set of positions of transmitters $\mathbf{T}_{N_T}(\mathbf{X}_\mathrm{T},\mathbf{Y}_\mathrm{T},\mathbf{Z}_\mathrm{T})$ and receivers $\mathbf{R}_{N_R}(\mathbf{X}_\mathrm{R},\mathbf{Y}_\mathrm{R},\mathbf{Z}_\mathrm{R})$, where N_T and N_R are the number of transmitters and receiver correspondingly. The reconstruction is performed for each of the selected pair of transmitter and receiver. In the case of TFM totally N_T * N_R pair are analysed. The reconstruction for each particular pair of transmitter and receiver is performed in the following steps:

1. The empty 3D array $\mathbf{I}_{\Sigma,N}(\mathbf{X},\mathbf{Y},\mathbf{Z})$is created for final image (integral image) with the number of points *N* and representing spatial area defined by $\mathbf{S}_N(\mathbf{X},\mathbf{Y},\mathbf{Z})$;
2. The empty 3D array $\mathbf{I}_{\mathrm{TR},N}(\mathbf{X},\mathbf{Y},\mathbf{Z})$is created for temporal image (Image created from a single pair of transmitter-receiver) with the number of points *N* and representing spatial area defined by $\mathbf{S}_N(\mathbf{X},\mathbf{Y},\mathbf{Z})$;
3. The one pair of transmitter and receiver from input data set is selected;
4. One of the space points from the $\mathbf{S}_N(\mathbf{X},\mathbf{Y},\mathbf{Z})$ is selected;
5. The coordinates of the point $P_{1\mathrm{T}}$ at which the beam from the transmitter to observation point crosses boundary between two media is determined according algorithm described in chapter 2.3.3;
6. The propagation time of the waves from transmitter to the observation point is estimated according:

$$t_\mathrm{T} = t_{\mathrm{T}1} + t_{\mathrm{T}2}, \tag{1.1}$$

where

$$t_{\mathrm{T}1} = \frac{1}{c_1}\sqrt{\left(x_T - x_{P_{1T}}\right)^2 + \left(y_T - y_{P_{1T}}\right)^2 + \left(z_T - z_{P_{1T}}\right)^2}\ , \tag{1.2}$$

$$t_{\mathrm{T}2} = \frac{1}{c_2}\sqrt{\left(x_O - x_{P_{1T}}\right)^2 + \left(y_O - y_{P_{1T}}\right)^2 + \left(z_O - z_{P_{1T}}\right)^2}\ ; \tag{1.3}$$

c_1 is the ultrasound velocity in the first media (water or wedge material); c_2 is the ultrasound velocity in the econd media (metal or other material of the component under inspection); x_T, y_T, z_T are the

coordinates of the selected transmitter; $x_{P_{1T}}, y_{P_{1T}}, z_{P_{1T}}$ are the coordinates of the point P_{1T}; x_O, y_O, z_O are the coordinates of the observation point.

7. In similar way the point P_{1R} is determined for the case of receiver. The propagation time of the waves of the observation point to the receiver is estimated according:

$$t_{\mathrm{R}} = t_{\mathrm{R1}} + t_{\mathrm{R2}}, \tag{1.4}$$

where

$$t_{\mathrm{R1}} = \frac{1}{c_1}\sqrt{\left(x_R - x_{P_{1R}}\right)^2 + \left(y_R - y_{P_{1R}}\right)^2 + \left(z_R - z_{P_{1R}}\right)^2}, \tag{1.5}$$

$$t_{\mathrm{R2}} = \frac{1}{c_2}\sqrt{\left(x_O - x_{P_{1R}}\right)^2 + \left(y_O - y_{P_{1R}}\right)^2 + \left(z_O - z_{P_{1R}}\right)^2}, \tag{1.6}$$

are the coordinates of the selected transmitter; $x_{P_{1R}}, y_{P_{1R}}, z_{P_{1R}}$ are the coordinates of the point P_{1R}.

8. The total propagation time is estimated as:

$$t_{\mathrm{TR}} = t_{\mathrm{T}} + t_{\mathrm{R}}, \tag{1.7}$$

9. The amplitude of the signals $u(t_{\mathrm{TR}})$ at time instance t_{TR} is estimated using linear interpolation between two neighbouring samples;
10. Obtained amplitude of the signal $u(t_{\mathrm{TR}})$ is assigned to the particular element of image array $\mathbf{I}_{\mathrm{TR},N}(\mathbf{X},\mathbf{Y},\mathbf{Z})$ which corresponds to the selected space point in the step 4.
11. The steps 4-10 are repeated until all elements of the image array $\mathbf{I}_{\mathrm{TR},N}(\mathbf{X},\mathbf{Y},\mathbf{Z})$ are estimated;
12. Completely estimated image $\mathbf{I}_{\mathrm{TR},N}(\mathbf{X},\mathbf{Y},\mathbf{Z})$ is added to the integral image $\mathbf{I}_{\Sigma,N}(\mathbf{X},\mathbf{Y},\mathbf{Z})$:

$$\mathbf{I}_{\Sigma,N}(\mathbf{X},\mathbf{Y},\mathbf{Z}) = \mathbf{I}_{\Sigma,N}(\mathbf{X},\mathbf{Y},\mathbf{Z}) + \mathbf{I}_{\mathrm{TR},N}(\mathbf{X},\mathbf{Y},\mathbf{Z}), \tag{1.8}$$

13. The steps 3-12 are repeated until pairs of transmitter - receiver are analysed;
14. Obtained images are analysed and presented in any desired projections.

2.3.3 Extension of the TFM for 0° incidence TRL

The classical TFM reconstruction method which was used to assess the FBH in previous section was extended for reconstruction in case of two media present – TRL wedge and the mockup. The task is illustrated by **Figure 18**.

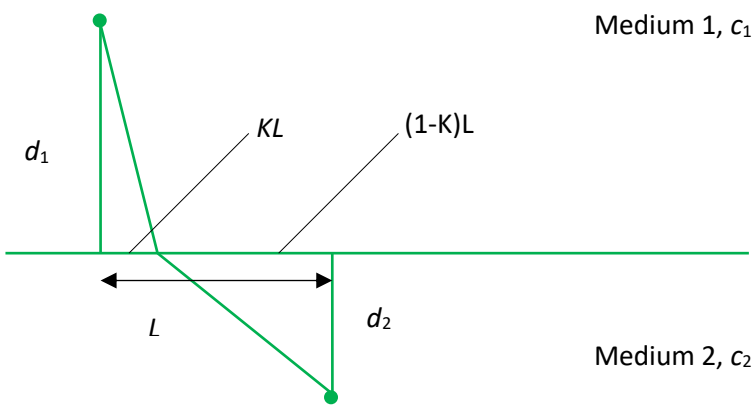

Figure 18: Illustration of the beam propagation through two media

According to Snell's Law:

$$\frac{c_1}{\sin(a_1)} = \frac{c_2}{\sin(a_2)}, \tag{1.9}$$

where c_1, c_2 are the ultrasound velocities in the first and second media corresponding; a_1, a_2 are the incident and refraction angles. It can be shown that:

$$\sin(a_1) = \frac{K \cdot L}{\sqrt{K^2 \cdot L^2 + d_1^2}}, \ \sin(a_2) = \frac{(1-K) \cdot L}{\sqrt{(1-K)^2 \cdot L^2 + d_2^2}}, \tag{1.10}$$

where d_1, d_2 are the distances (perpendicular) from incident and observation points to the boundary (plane) separating two media; L is the distance between points where perpendiculars crosses media separating plane; $K \in [0 \div 1]$ is the virtual coefficient determining how the line between perpendiculars are divided by the beam cross-section point. So the general equation for the determination of the beam cross-section point is:

$$\frac{c_2 \cdot K \cdot L}{\sqrt{K^2 \cdot L^2 + d_1^2}} = \frac{c_1 \cdot (1-K) \cdot L}{\sqrt{(1-K)^2 \cdot L^2 + d_2^2}}. \tag{1.11}$$

The distances d_1, d_2 to the plane are determined according:

$$d_1 = \frac{A \cdot x_{in} + B \cdot y_{in} + C \cdot z_{in} + D}{\sqrt{A^2 + B^2 + C^2}}, \ d_2 = \frac{A \cdot x_o + B \cdot y_o + C \cdot z_o + D}{\sqrt{A^2 + B^2 + C^2}}, \tag{1.12}$$

where A, B, C, D are coefficients determining in 3D space the plane separating two media; x_{in}, y_{in}, z_{in} are the coordinates of the incident point; x_o, y_o, z_o are coordinates of the observation point. The coordinates of the projection incident and observation points on the plane can be determined according to:

$$\begin{aligned} x_{in,p} &= x_{in} - d_1 \cdot \frac{A}{\sqrt{A^2 + B^2 + C^2}} \\ y_{in,p} &= y_{in} - d_1 \cdot \frac{B}{\sqrt{A^2 + B^2 + C^2}} \\ z_{in,p} &= z_{in} - d_1 \cdot \frac{C}{\sqrt{A^2 + B^2 + C^2}} \end{aligned} \tag{1.13}$$

$$\begin{aligned} x_{o,p} &= x_o - d_2 \cdot \frac{A}{\sqrt{A^2 + B^2 + C^2}} \\ y_{o,p} &= y_o - d_2 \cdot \frac{B}{\sqrt{A^2 + B^2 + C^2}}. \\ z_{o,p} &= z_o - d_3 \cdot \frac{C}{\sqrt{A^2 + B^2 + C^2}} \end{aligned} \tag{1.14}$$

The distance between these two projections can be determined using:

$$L_{P12} = \sqrt{(x_{in,p} - x_{o,p})^2 + (y_{in,p} - y_{o,p})^2 + (z_{in,p} - z_{o,p})^2}. \tag{1.15}$$

Then the position of the point satisfying Snell's law can determined as distance along line L_{P12} from the projection of the origin point $x_{o,p}$, $y_{o,p}$, $z_{o,p}$ on the plane separating two media:

$$L_{Snell} = \min_k \left[\left| c_2^2 \cdot \frac{(kL_{P12})^2}{(kL_{P12})^2 + d_1^2} - c_1^2 \cdot \frac{((1-k) \cdot L_{P12})^2}{((1-k) \cdot L_{P12})^2 + d_2^2} \right| \right], \tag{1.16}$$

where c_1, c_2 are the ultrasound velocity in the first and second media; .

The propagation time of ultrasonic beam along path through point L_{Snell} is obtained as:

$$t_1 = \frac{\sqrt{L_{Snell}^2 + d_1^2}}{c_1}$$
$$t_2 = \frac{\sqrt{(L_{12} - L_{Snell})^2 + d_2^2}}{c_2} \quad (1.17)$$

The extension of the classical TFM for reconstruction in case of two media present was verified with CIVA, employing simple model with FBH. In the model, the FBH having a diameter of 5mm and ligament of 45mm was created as illustrated in Figure 19. The sample was a rectangular block made of stainless steel with dimensions 300mm×100mm×90mm. The 1MHz 32 element phased arrays in TRL configuration of 0° incidence and 10° roof angle were used for FMC acquisition. The sketch of the model is presented in Figure 19.

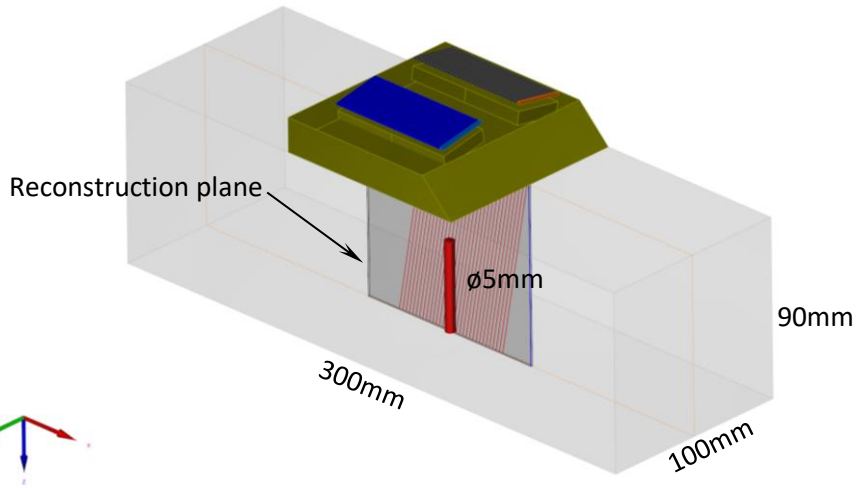

Figure 19: The sketch of the CIVA model used for verification of TFM reconstruction in case of two media present

For verification purposes the TFM reconstruction at the specified plane (Figure 19) was performed using CIVA and then using custom implemented technique, described above. The comparison of reconstruction results can be seen in Figure 20.

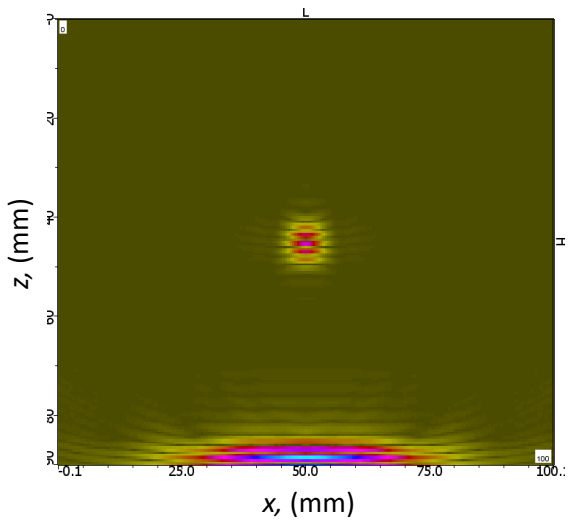

a)

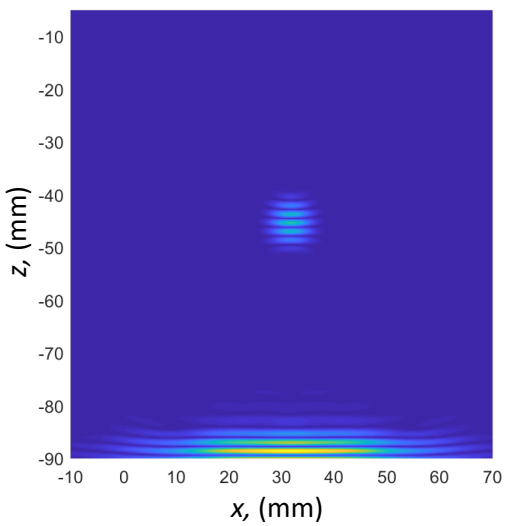

b)

Figure 20: The TFM reconstruction in case of two media using CIVA (a) and custom implemented technique (b)

2.3.4 Extension of the TFM for TRL on convex samples

In the case when the boundary between two media is cylindrical (pipes) the task is solved in the following way (Figure 21):

- The assuming that the boundary is planar the beam cross-section point P_0 is determined in the way described above and:

$$\begin{aligned} P_{0x} &= x_{in,p} + \left(x_{o,p} - x_{in,p}\right)\cdot k_{\min} \\ P_{0y} &= y_{in,p} + \left(y_{o,p} - y_{in,p}\right)\cdot k_{\min} \\ P_{0z} &= z_{in,p} + \left(z_{o,p} - z_{in,p}\right)\cdot k_{\min} \end{aligned} \tag{1.18}$$

- Vertical projection P_1 of the point P_0 to the cylindrical plane is determined:

$$\begin{aligned} P_{1x} &= P_{0x} \\ P_{1y} &= P_{0yx} \\ P_{1z} &= -\left(R_{\text{cyl}} - \sqrt{R_{\text{cyl}}^2 - P_{0y}^2}\right) \end{aligned} \tag{1.19}$$

- The coefficients of the new plane which tangential to the cylindrical boundary at the point P_1 are determined:

$$\begin{aligned} A_1 &= A, \\ B_1 &= P_{1y}, \\ C_1 &= P_{1z} + R_{cyl}, \\ D_1 &= -\left(A_1 \cdot P_{1x} + B_1 \cdot P_{1y} + C_1 \cdot P_{1z}\right). \end{aligned} \tag{1.20}$$

- Then the determination of the new point P_0 on the plane A_1, B_1, C_1, D_1 stultifying Snell's law is determined using procedure described above and the steps 1-3 repeated again. The verification has demonstrated that repeating of this procedure 2-3 times gives sufficient accuracy for SAFT reconstruction.

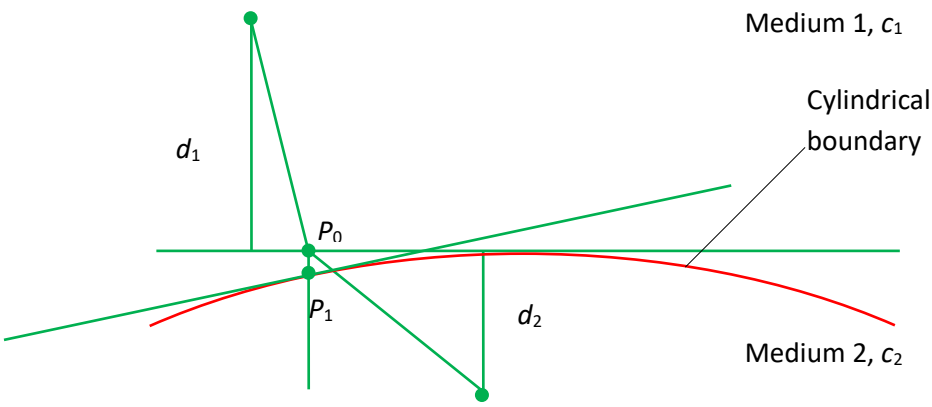

Figure 21: Illustration of the beam propagation through two media with cylindrical boundary

2.3.5 PE-TFM measurements

In order to collect reference data that will be compared to TRL reconstructions, the experiments were carried out with a single array in pulse echo (PE-TFM) mode without the TRL wedge. The array was positioned directly on the surface of (**RDIM3**) sample and standard full matrix capture data acquisition was applied with a 0° linear array. After the experiment, the data from the samples were reconstructed using the classic total focusing method. The reconstructions from this experiments are further referenced as PE-TFM. The experiments were carried out using a 1MHz 32 element phased array, the same which will be further used for TRL acquisitions. In each case, the data was acquired at discrete array offsets from the left egde of the mock-up (not a continuous scan with encoder), where each offset corresponds to the center of the FBH. The experimental set-up is presented in Figure 22. The array offsets from the edge of sample are summarized in Table 4. In the experiment, the FBH defects referenced as C, D and E were measured, as they are located at depths of 40mm to 80mm.

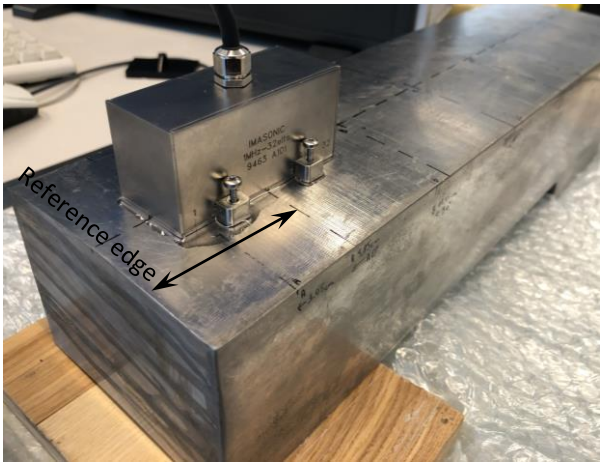

Figure 22: PE-TFM set-up using 1MHz 32 element phased array

Table 4: The offsets of the center of the array from the reference edge of the sample

Defect reference	C	D	E
Array offset from reference edge (mm)	178.5	238.5	336.5

The reconstructed PE-TFM images from the sample in case of the 1MHz 32 element array measurements are presented in Figure 1.23. From results presented below it can be seen that the FBHs referenced as C and D can be reconstructed from direct contact PE-TFM measurements with approximate signal to noise ratio of 8dB. The SNR here is defined as a peak-to-peak signal to noise ratio, where noise is calculated from the region above the defect and the signal value is estimated at the reconstructed defect position. The FBH located at a depth of 80mm (E) was not successfully reconstructed, possibly due to high structural noise and high attenuation in the coarse grained structure. Previous measurements show that the attenuation in the sample (**RDIM3**) is approx. 180dB/m at 1MHz. As a result, for the particular mock-up 60mm depth sets a limit for a standard PE-TFM reconstruction at 1MHz.

 © ADVISE consortium

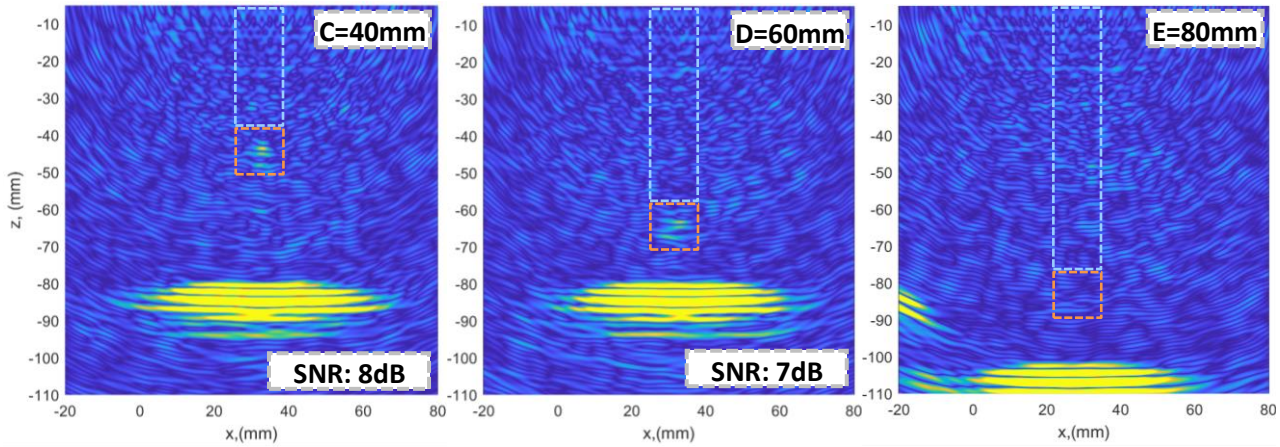

a) b) c)

Figure 23: The 0° TFM reconstruction of FBH C (a), D (b) and E (c) using 1MHz 32 element phased array

2.3.6 Comparison of PE-TFM and TRL-TFM

In this section, the comparison between PE-TFM obtained in pulse-echo mode and TFM on 0° incidence TRL (TRL-TFM) is presented. In both experiments, the same hardware settings were used: excitation voltage 100 V, gain 60 dB, sampling frequency 40 MHz. The reconstructed FBH in case of PE-TFM measurements can be seen in Figure 25a-c. Note that this replicates the results presented in Figure 23. Meanwhile, the TRL-TFM reconstruction is presented in Figure 25d-f.

Note that reconstructions presented in Figure 25 were made presuming that the surface of the sample is flat. In addition, the scales of PE-TFM and TRL-TFM images are not the same, however both images can be compared in terms of SNR.

Another important aspect is that throughout the TRL data acqusition, the reversed excitation was used to reduce electrical noise and internal noise of the particular element of phased array. This means that two FMC acquisitions were made, changing the order of transmitting and receiving arrays (Figure 24).

Then, to obtain combined FMC matrix, each signal was created selecting minimal sample value between two corresponding datasets:

$$y_{n_i,k_j}(t_m) = \begin{cases} y_{1,n_i,k_j}(t_m) & if \ \left|y_{1,n_i,k_j}(t_m)\right| < \left|y_{2,n_i,k_j}(t_m)\right| \\ y_{2,n_i,k_j}(t_m) & otherwise \end{cases} \tag{1.21}$$

where $y_{n_i,k_j}(t_m)$ – is the output magnitude value of ith and j^{th} signal at time instance t_m, $y_{1n_i,k_j}(t_m)$ and $y_{2n_i,k_j}(t_m)$ – are the magnitude values of at point (i,j) at time instance t_m that correspond to the first and second FMC acquisition respectively, i=1,...I, where I is the total number of measurement positions on n axis, j=1,...J, where J is the total number of measurement positions on k axis, m=0,...M, where M is the number of samples of the signal. The availability of this acquisition technique is one of the advantages of TRL-TFM over the PE-TFM measurement. In case of PE-TFM mode, many signals require to be averaged in order to achieve at least a similar suppression of electrical noise.

Two main observations can be made from the results presented in Figure 25:

1. First, the SNR at the beam convergence point (62.6mm) is higher for the TRL-TFM measurement than in the PE-TFM method, which confirms the initial idea of reduced backscatter volume for TRL set-ups. This can be observed form Fig. 25b and Fig. 25e. The conventional PE-TFM measurement shows better performance for subsurface defects, which can be seen from Fig. 25a and Fig. 25e. On the other hand, SNR in case of PE-TFM significantly decreases when going deeper into the material (Fig. 25b-c). In contrast, TRL-TFM shows an increased SNR at the beam convergence point (Fig. 25e) and an overall decrease of structural noise at the locations outside the beam convergence area.

2. Second, the reconstruction depth in case of TRL-TFM can be increased, as a hole located at a depth of 80mm can be detected (Fig. 25f). The acquisitions from PE-TFM mode (Fig. 25c) demonstrate that TFM was unable to distinguish such a defect. As a result, TRL-TFM provides increased inspection depths and increased SNR at beam convergence point in comparison to conventional PE-TFM measurement.

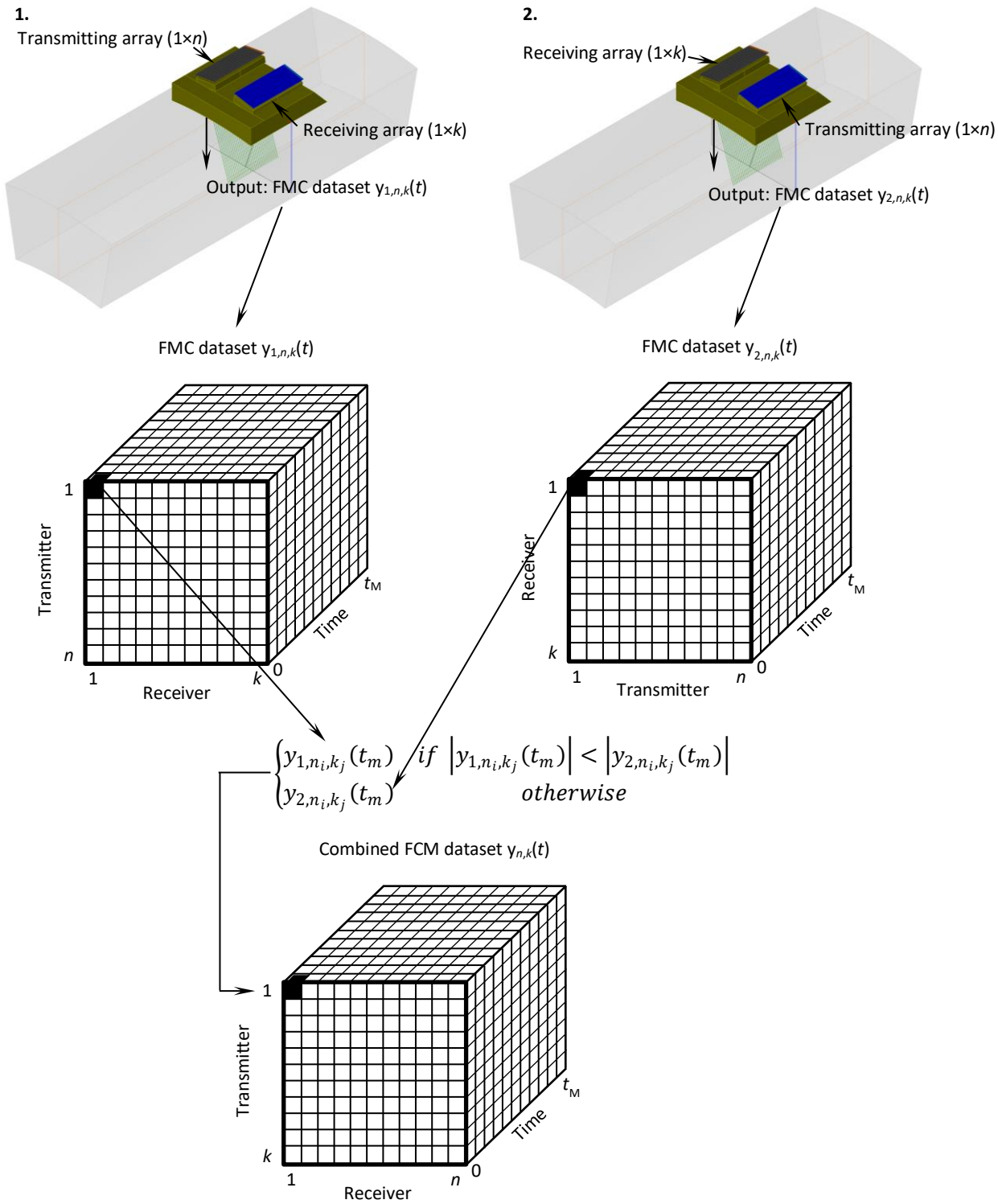

Figure 24: Explanation of the reversed excitation and estimation of the combined FMC dataset from two separate FMC acquisitions

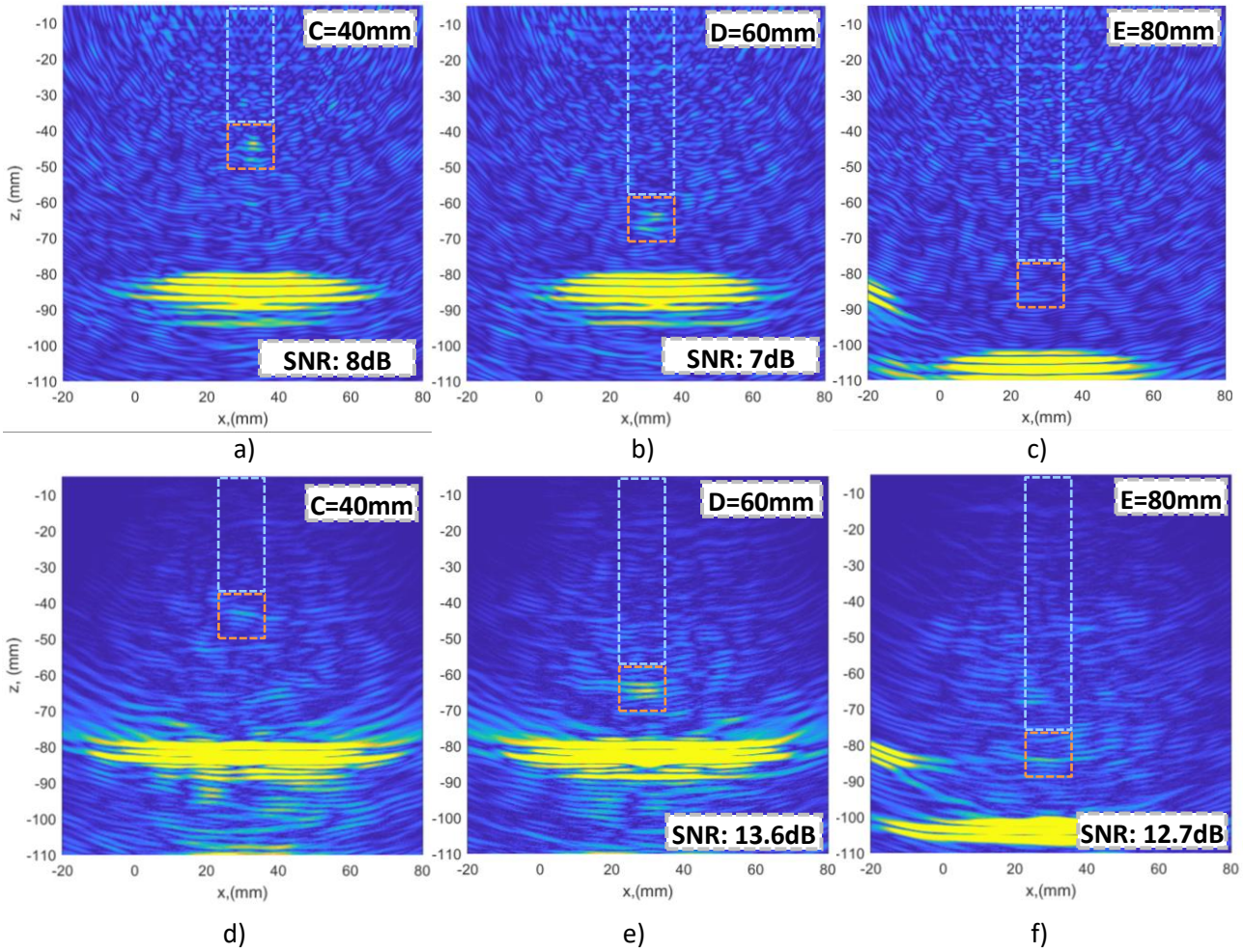

Figure 25: The PE TFM reconstruction of FBH C (a), D (b) and E (c) and TFM reconstruction of FBH C (d), D (e) and E (f) with 0° incidence TRL

The results presented above demonstrate that TRL-TFM improves SNR within the beam convergence region. As this beam intersection area is quite large and covers approximately 40mm, defects that fall into this region can all be detected with improved SNR compared to PE-TFM measurement. It can also be observed that in case of PE-TFM the noise is homogenous in all reconstruction plane (Fig. 25a-c). Meanwhile, in case of TRL-TFM the noise outside the beam convergence area is supressed, which demonstrates that the volume of material which contributes to the back-scattered noise is significantly reduced in case of TRL-TFM (Fig. 25d-f). Finally, the TRL-TFM set-up brings more flexibility for defect assessment. For example, using 0° incidence TRL wedges with matrix arrays it is possible to change the beam convergence depth dynamically by adjusting delay times of array elements. In this case, the beam can be dynamically focused at different depths of the material, while at the same time maintaining reduced backscatter volume. On the other hand, both linear and matrix arrays can be used with 0° incidence TRL wedges to steer the beam in frontal direction, achieving different incidence angles. As a result, one wedge could be used instead of a set of wedges for longitudinal wave focusing at particular depth and incidence angle.

2.3.7 Extension of the TFM for classical TRL

In addition to the experiments presented in the previous section, the acquisitions on sample (**1618-B359-B3**) were made using conventional TRL wedges having both incidence and roof angles. In this case, the sample had a flat surface, hence the flat surface conventional TRL wedge was used having roof angle of 10° and incidence angle of 8°. The TFM reconstruction results from the TRL set-up were then compared to 0° PE-TFM. In both cases, the same hardware settings were maintained: excitation voltage 100 V, gain 40 dB, sampling

frequency 40 MHz. The reconstructed SDH defects using the TRL-TFM method in case of a conventional TRL acquisition are presented in Figure 26a, while the 0° PE-TFM reconstruction can be seen in Figure 26b. The results presented below demonstrate that in both cases the indications of defects can be clearly observed. Conventional TRL measurements provide larger reconstruction volume in contrast to conventional 0° PE-TFM measurement. As it can be seen from Fig. 26a, conventional TRL enables to extend the reconstruction plane in horizontal direction in comparison to PE-TFM (Fig. 26b). Apart from that, TRL does not provide any additional value in detection of SDH if the backscattering noise is not very high in the investigated material. As it was shown in the previous section, the added value of the TRL starts to appear when the average grain size of the structure is at least one third of the wavelength.

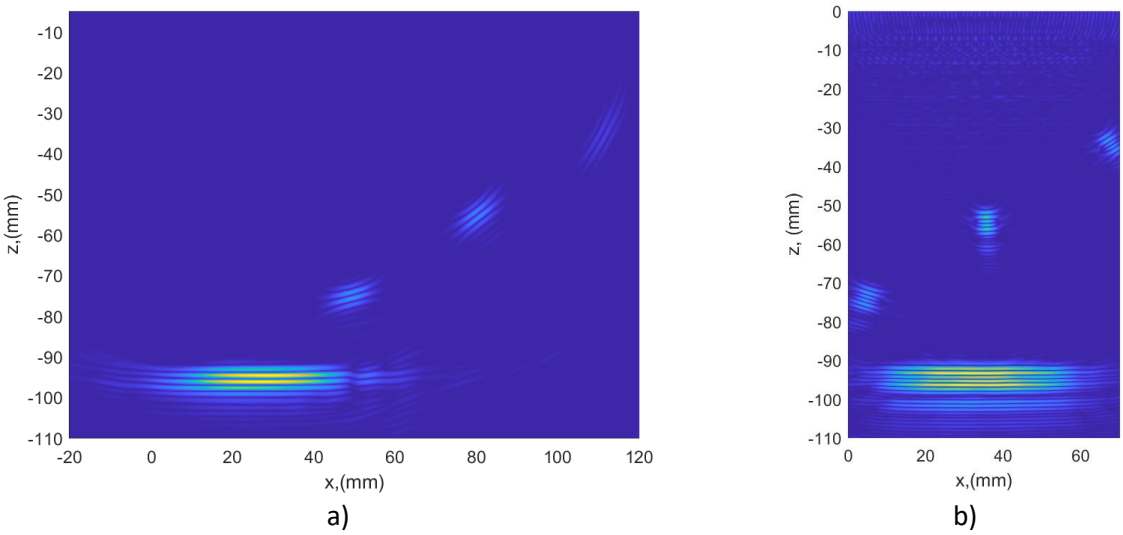

Figure 26: The comparison between the reconstruction using classical TRL wedge (a) and 0° PE TFM (b)TRL phased array imaging

3 Super resolution imaging and phase coherence TFM

This section was conducted by Imperial College London (ICL) and has two aims:

- to comment on the usefulness of Super Resolution (SR) algorithms for inspection of coarse-grained components.
- to demonstrate the findings on the TRL dataset collected by the team at KTU, Lithuania.

This section focuses on the time-reversal multiple signal classification algorithm (TR-MUSIC), which is one of the most popular in the field [1]. As an alternative, the correction to classical total focusing method (TFM) offered by phase coherence information is discussed [2].

3.1.1 Motivation to use TRL set-ups and SR algorithms

For coarse-grained materials, structural noise covers most defect signatures rendering images illegible. The ultimate challenge for the inspection of such components is to enhance the signal-to-noise ratio (SNR), which is also at the core of this report.

The TRL setup improves the SNR, since it minimises the contribution of backscattered ultrasound in the recorded signals. Consequently, defect signatures can stand out more clearly from the noise background. On the other hand, SR algorithms allow for a refinement of an ultrasonic array image of a small area, with an a priori knowledge of the defect location. The main motivation for using super resolution methods is to size defects or infer their shape [3]. They are known to perform poorly in noisy configurations and are typically suitable only when SNR is above 20 dB [4] - a scenario often not available in coarse-grained components. However, a possible way to benefit from super resolution algorithms in this context is to lower the frequency of inspection. This in turn reduces the backscatter creating a potentially favourable environment for SR methods which can potentially compensate for the loss of resolution related to lower frequency.

3.1.2 Leveraging the phase of the signals

While the backscatter is less significant for lower frequencies, it is often difficult to achieve the above stated SNR of 20 dB. In recent years, several authors opened the SR algorithms to noisy structures by utilising the phase of the signals [5, 6, 7, 8]. Unlike in classical TR-MUSIC, the phase coherent variant maintains the phase information while adding contributions of multiple frequencies. Consequently, they improve the signatures of true scatterers, at which the phases are coherent.

The SR images are often compared against the total focusing method (TFM). The phase coherence has also been used with the TFM offering promising enhancements [2, 9, 10]. For noise-free materials, the TFM with the phase coherence correction gains some super-resolution features, while for grained materials it has been shown to improve the SNR significantly.

This section demonstrates the application of SR methods to coarse-grained materials, including the phase-coherent variant. The results are compared to the classical TFM and the TFM with the phase coherence correction. The theory of one of the most popular SR methods - TR-MUSIC - and of the concept of phase coherence correction to TFM are briefly reviewed first. Then, we illustrate the application challenges with examples computed from finite element simulations of models with increasing grain size. Finally, the methods are applied to experimentally collected TRL datasets.

3.2 A brief review of the theory of TR-MUSIC

TR-MUSIC imaging is based on the observation that in the absence of multiple scattering, the information about discrete scatterers is contained in the eigenvalues and eigenvectors of the time reversal operator. Devaney et al. [1] has shown the equivalence of the eigenspectrum of the time reversal operator and the

singular value decomposition of the multistatic response matrix. Resulting singular values and singular vectors can be split into two subspaces: the signal subspace and the noise subspace. The former contains information related to the scatterers. For noise-free data, the distinction between the two is sharp, but if structural noise is present, the scatterer information is spread between multiple values and the separation is much less clear.

The multistatic response matrix (which is the full matrix capture dataset in the frequency domain) is symmetric, so its SVD can be written as

$$\mathbf{K}(\omega) = \mathbf{U\Sigma V}^{\mathrm{H}} = \mathbf{U\Sigma U}^{\mathrm{T}} \tag{2.1}$$

where

$$\begin{aligned} \mathbf{U}^{\mathrm{T}}\mathbf{U} &= \mathbf{I} \\ \mathbf{V}^{\mathrm{H}}\mathbf{V} &= \mathbf{I} \end{aligned} \tag{2.2}$$

The singular vectors can be divided into two subspaces, the signal subspace $\mathbf{U}_s$, $\mathbf{V}_s$ and the noise subspace $\mathbf{U}_n$, $\mathbf{V}_n$. If point scatterers are present, their Green's functions $\mathbf{g}(\mathbf{r})$ are among the singular vectors belonging to the signal subspace. Consequently, one can verify whether a particular point at $\mathbf{r}$ is a scatter by verifying the relationship between its Green's function and $\mathbf{U}_s$. The Green's function between a point located at $\mathbf{r}_x$ and an ith array element at $\mathbf{r}_i$ may be approximated as

$$\mathbf{g}(\mathbf{r}_x, i) = e^{-jk|r_i - r_x|} \tag{2.3}$$

The complete Green's function vector for all N array elements at point $\mathbf{r}_x$ is

$$\mathbf{G}(\mathbf{r}_x) = [\mathbf{g}(\mathbf{r}_x, 1) \quad \mathbf{g}(\mathbf{r}_x, 2) \quad \cdots \quad \mathbf{g}(\mathbf{r}_x, N)]^{\mathrm{T}} \tag{2.4}$$

The key `test' of TR-MUSIC is the inner product $\boldsymbol{U}_s^{\mathrm{H}}\mathbf{G}(x)$ which vanishes if there is no match between the Green's function vector and the singular vectors at a given frequency.

TR-MUSIC images can be constructed either using the signal or the noise subspace. If the signal subspace is used, the image is calculated as

$$I(\mathbf{r}_x, \omega) = \left|\frac{1}{1 - A(\mathbf{r}_x, \omega)}\right| \tag{2.5}$$

where

$$A(\mathbf{r}_x, \omega) = \frac{\mathbf{G}(\mathbf{r}_x, \omega)^{\mathrm{H}}\mathbf{U}_s\mathbf{U}_s^{\mathrm{H}}\mathbf{G}(\mathbf{r}_x, \omega)}{\|\mathbf{G}(\mathbf{r}_x, \omega)\|} \tag{2.6}$$

The numerator in the expression for operator $A(\mathbf{r}_x, \omega)$ is the inner product of a vector and its conjugate transpose which makes the operator real. If the noise subspace is used, the imaging function takes a different form

$$I(\mathbf{r}_x, \omega) = \left|\frac{1}{A(\mathbf{r}_x, \omega)}\right| \tag{2.7}$$

which follows from the relationship between the singular vectors in equation (2.2).

The imaging function can be calculated at a single frequency corresponding to the centre frequency of the transducer but it can also be calculated over a frequency band, summing all the contributions. In that case, it takes the form

$$I(\mathbf{r}_x, \Delta\omega) = \left|\frac{1}{1 - \frac{1}{N}\sum_i^N A(\mathbf{r}_x, \omega_i)}\right| \tag{2.8}$$

This variant is often referred to as the multi-frequency TR-MUSIC (MF-TR-MUSIC).

3.2.1 Phase-coherent TR-MUSIC

The form of (2.6) indicates that only the amplitude information is retained in the calculation and summed later in the imaging function (2.8). Over the recent years, several authors made use of that information to improve the quality of the images [5, 6, 7]. A slight modification to (2.6) allows for the phase to be retained

$$A(\mathbf{r}_x, \omega) = \frac{\mathbf{G}(\mathbf{r}_x, \omega)^{\mathrm{H}} \mathbf{U}_S \mathbf{U}_S^{\mathrm{T}} \mathbf{G}^*(\mathbf{r}_x, \omega)}{\|\mathbf{G}(\mathbf{r}_x, \omega)\|} \tag{2.9}$$

When used in the multi-frequency imaging function (2.8) it enhances the true scatterers' signatures whose phases add coherently over the chosen frequency bands. The benefits of the phase-coherent TR-MUSIC (PC-MUSIC) will be demonstrated using the examples in the next section. Note that the phase-coherent algorithm is always used at multiple frequencies in this chapter.

3.3 Phase coherence imaging as a correction to classical TFM

The phase coherence information can also be used directly with FMC data, without the need of relatively complicated processing required for TR-MUSIC. A classical TFM image is calculated as

$$I_{\mathrm{TFM}}(\mathbf{r}_x) = \left| \sum_{i}^{N_t} \sum_{j}^{N_r} \mathcal{H} y_{i,j}[\tau(\mathbf{r}_x)] \right| \tag{2.10}$$

where N_t and N_r are the numbers of transmitting and receiving array elements, $y_{i,j}[\tau(\mathbf{r}_x)]$ is the time trace recorded at element j when element i is transmitting and interpolated at time $\tau(\mathbf{r}_x)$, which is the delay law for the i, j transducers configuration at location $\mathbf{r}_x$ in the imaging domain.

Camacho et al. [2] pointed out that the coherence of phase for different transducer pairs associated with true scatterers can be used to enhance the image. They proposed three correction factors: circular coherence, phase coherence and sign coherence. The corresponding expressions are shown below:

$$\mathrm{CCF}(\mathbf{r}_x) = \sqrt{1 - \mathrm{var}\big(\cos\varphi(i,j,\mathbf{r}_x)\big) + \mathrm{var}\big(\cos\varphi(i,j,\mathbf{r}_x)\big)} \tag{2.11}$$

$$\mathrm{PCF}(\mathbf{r}_x) = \max\left[0, \frac{\mathrm{std}\big(\varphi(i,j,\mathbf{r}_x)\big)}{\sqrt{\pi/3}}\right] \tag{2.12}$$

$$\mathrm{SCF}(\mathbf{r}_x) = 1 - \sqrt{1 - \mathrm{mean}\left(\mathrm{sgn}\big(y_{i,j}[\tau(\mathbf{r}_x)]\big)\right)} \tag{2.13}$$

where $\varphi(i,j,\mathbf{r}_x)$ is the phase of $y_{i,j}[\tau(\mathbf{r}_x)]$.

The final image containing phase coherence information are a product of the classical TFM image and the correction factor, for instance:

$$I_{\mathrm{CCF}}(\mathbf{r}_x) = I_{TFM}(\mathbf{r}_x)\mathrm{CCF}(\mathbf{r}_x) \tag{2.14}$$

3.4 Simulated examples

To demonstrate the strengths and weaknesses of these methods, we first use a few simulated examples with increasing grain size (average diameters between 0.5 and 2 mm). The microstructures were generated as a Poisson-Voronoi distribution using *neper* and were assigned random cubic crystal orientations.

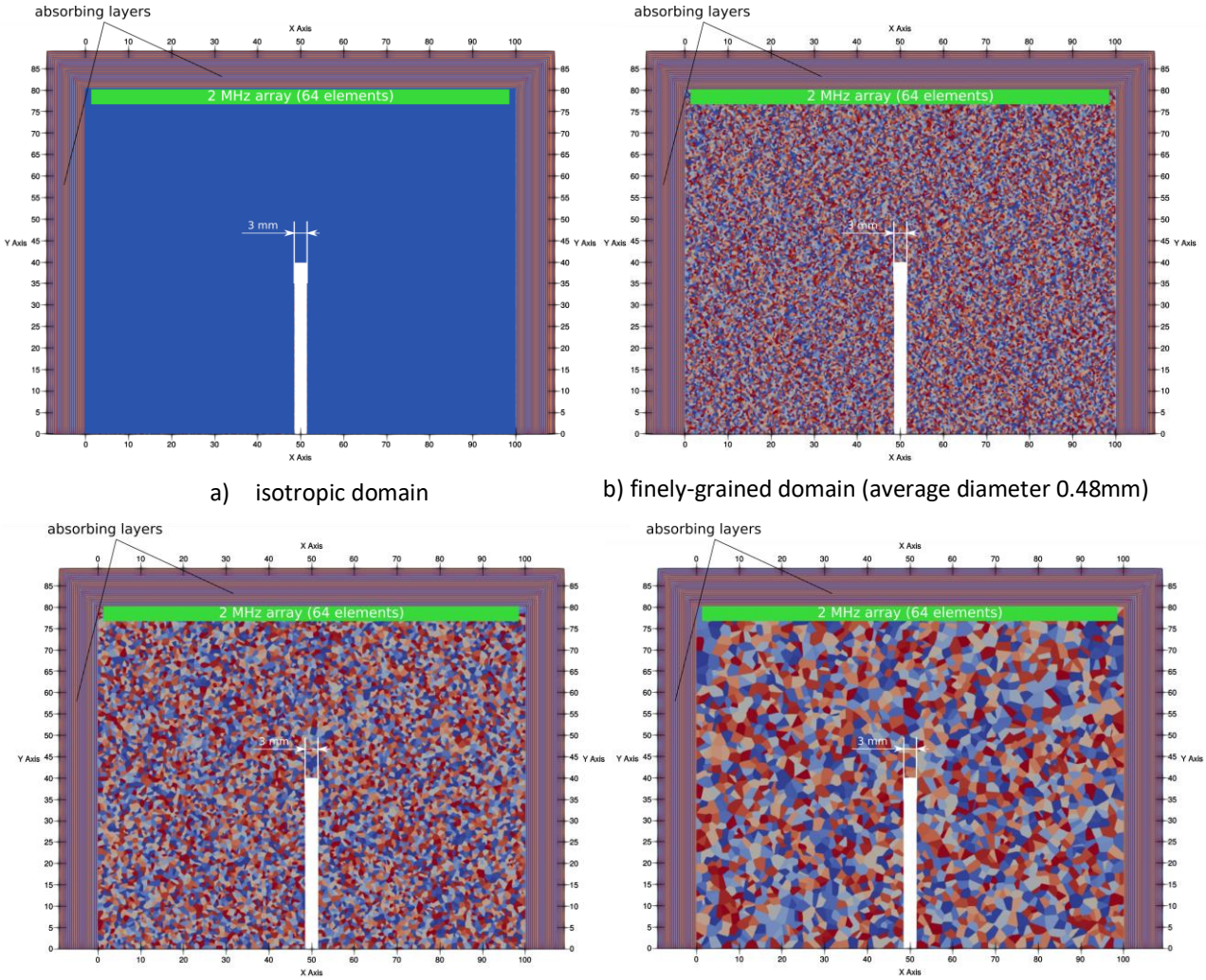

a) isotropic domain

b) finely-grained domain (average diameter 0.48mm)

c) coarsely grained domain (average diameter 0.96mm)

d) very coarsely-grained domain (average diameter 1.95mm)

Figure 27: Finite element models used in the comparison

We consider a 100 × 80 mm 2D model with a notch, imaged using a 64 elements 2 MHz array and surrounded by absorbing layers to minimise reflections from boundaries. The material properties for the isotropic model are E = 194.6 GPa, υ=0.3, and ρ=7958 kg/m^3, whereas for the grained models c_{11} = 206.7 GPa, c_{12} = 134 GPa and c_{44} = 113.5 GPa, and ρ=7958$ kg/m^3. The notch is 3 mm wide and 40 mm tall and is located at the middle of the length of the model. Schematic diagrams depicting the grain structures are shown in Figure 27.

3.4.1 Comparison metrics and scaling conventions

Array images below are compared with respect to two metrics, the signal to noise ratio (SNR) and the contrast to noise ratio (CNR). In all cases the region of interest (ROI) is 20×20 mm square; the signal part is contained in the central 4×4 mm part, whereas the noise is calculated over the whole ROI except for the signal square. The definitions for SNR and CNR are as follows:

$$\mathrm{SNR(dB)} = 20\log_{10}\frac{\max(\mathrm{signal})}{\sqrt{\mathrm{mean}(\mathrm{noise}^2)}} \tag{2.15}$$

$$\mathrm{CNR(dB)} = 20\log_{10}\frac{\max(\mathrm{signal}) - \mathrm{mean}(\mathrm{noise})}{\mathrm{std}(\mathrm{noise})} \tag{2.16}$$

It is also important to note that the comparison below only includes the above-defined metrics and cannot be seen as fully comprehensive. Its purpose is to illustrate how different imaging approaches perform on the given datasets. A more rigorous comparison should include a probability-of-detection study, which is beyond the scope of this report.

All SR images are scaled with respect to the maximum of the image (0 dB). The lower limit for image values is dictated by the minimum of each particular image. On the contrary, TFM images are always shown with a chosen value range, most often from 0 to -40 dB, except for the very coarsely-grained case, where a lower limit of -6 db was used.

3.4.2 Isotropic material

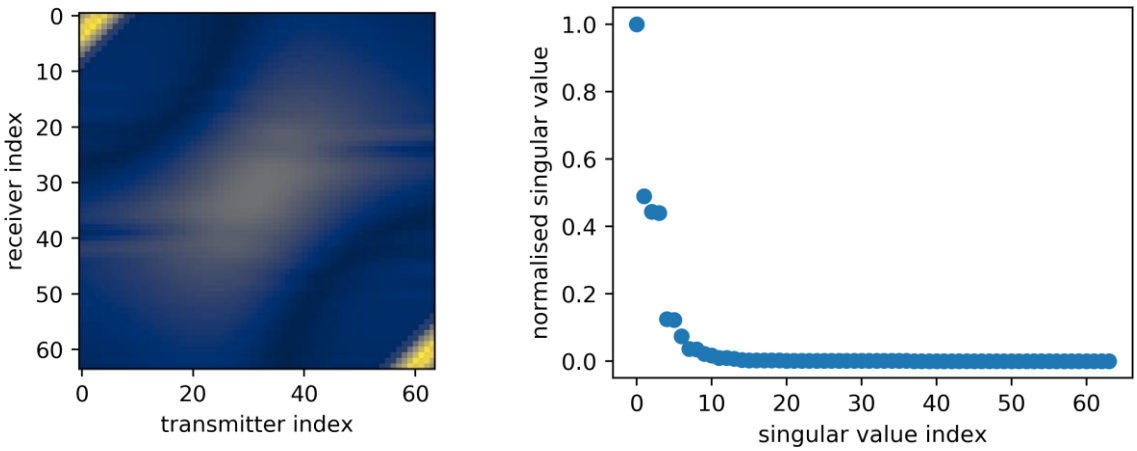

a) $|\mathbf{K}(\omega)|$

b) Singular values

Figure 28: The multistatic response matrix at the centre frequency of 2 MHz

The basic steps for TR-MUSIC are shown first for isotropic materials. With no structural noise present, we expect high SNR without any special treatment. The multistatic response matrix $\mathbf{K}(\omega)$ is obtained by applying the FFT to the time-domain FMC dataset. Typically, the FMC data is first gated so that only the portion of the time history thought to correspond to the region of interest is retained. TR-MUSIC is essentially a post-imaging method, which requires some a priori knowledge of the approximate location of the defect. SR image is then computed over a small area which is the region of interest.

Matrix $\mathbf{K}(\omega)$ at the centre frequency of the excitation is shown in Figure 28a and its singular values in Figure 28b. Note that the division between the signal and noise subspaces is very clear. Having performed the singular value decomposition, the images can be generated following the procedure explained in Eqs. 2.8–2.9.

3.4.2.1 SR images

The MUSIC images for the isotropic case are shown in Figure 29 and compared to the classical TFM image shown in Figure 29a. The SR image computed at a central frequency offers lower overall SNR, but the signatures of the corners of the FBH better pronounced (albeit slightly mislocated). Combining results from a wider frequency band further reduces the comparison metrics. However, the phase-coherent version shown in Figure 29d shows excellent vertical resolution and very high CNR. The noise floor of this image is significantly higher as compared to the TFM image, but it is fairly flat and does not conceal the signature of the defect.

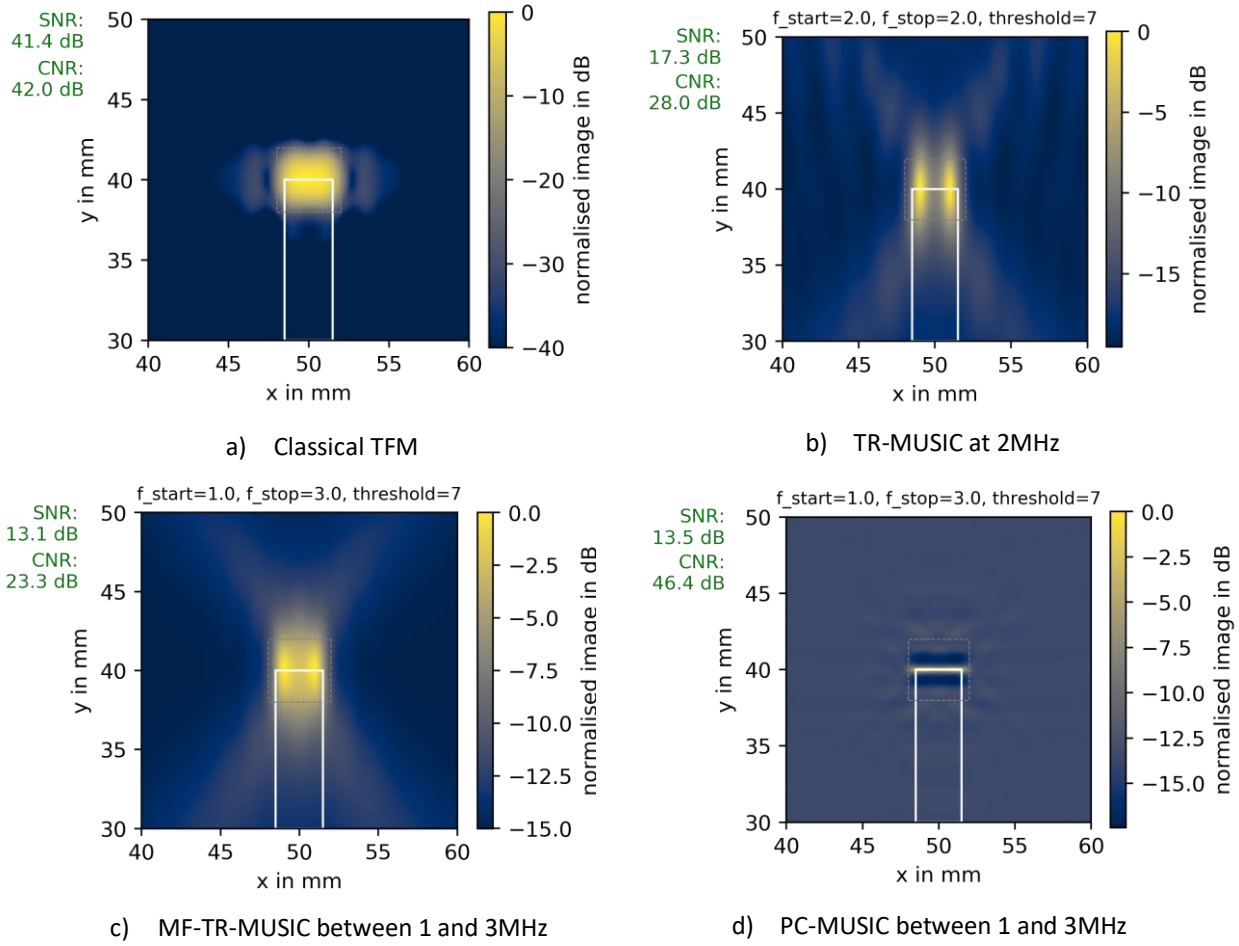

Figure 29: SR images for the isotropic case

The TFM images with phase coherence corrections are displayed in Figure 30. The improvement in both the SNR and CNR is very significant for all correction factors. In addition to that, the CCF variant shows improved lateral resolution, with two peaks corresponding to the tips of the notch better pronounced (like in SR images). The PCF and SCF variants improve vertical resolution, however they suffer from side lobes. The comparison metrics are summarised in Table 5 for convenience.

Table 5: The comparison of SNR and CNR for the isotropic model

test case/imaging method		TFM				TR-MUSIC		
		Classical	CCF	PCF	SCF	CF		PC
isotropic	SNR	41.4	60	60.2	68.4	17.3	13.1	13.5
	CNR	42	60.3	60.3	68.6	28	23.3	46.4

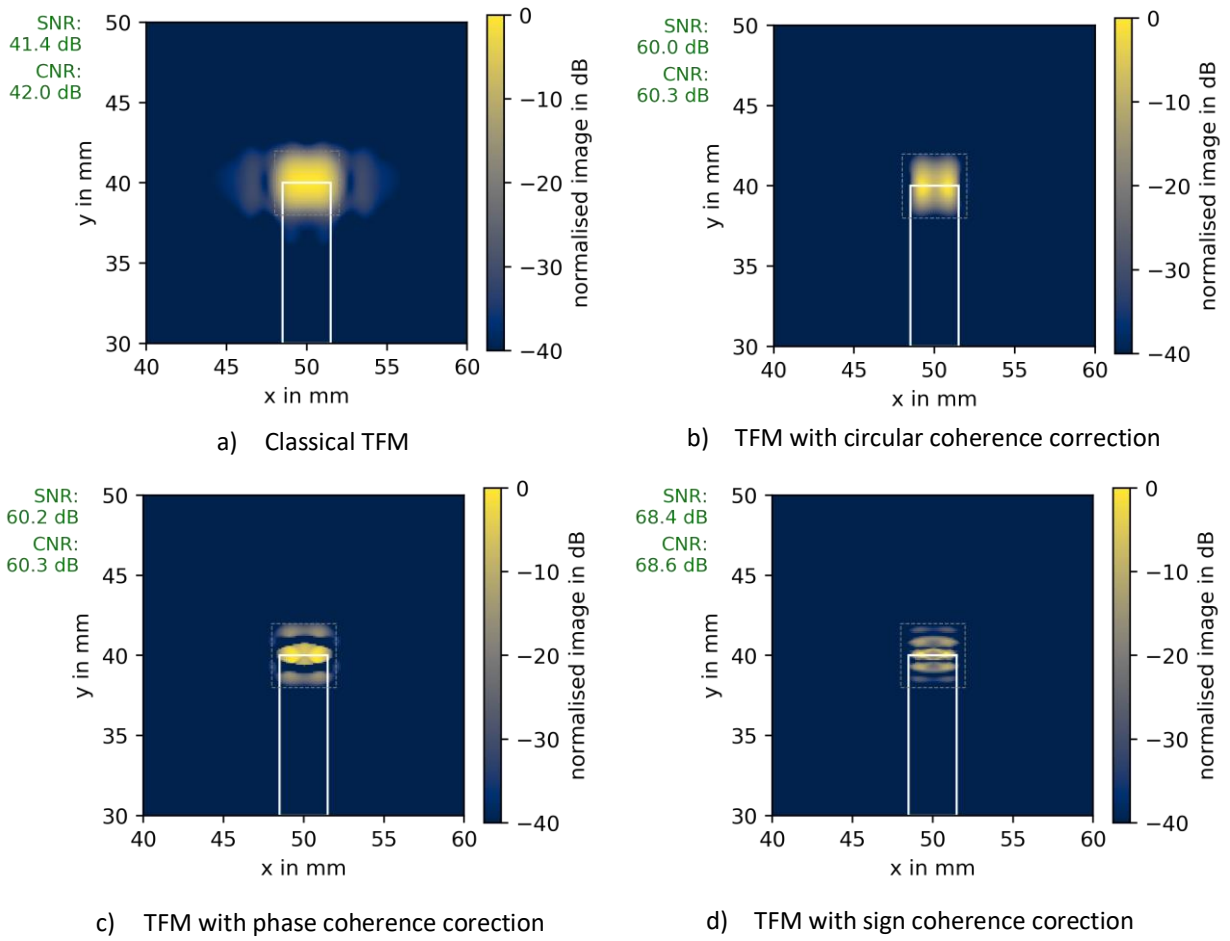

a) Classical TFM

b) TFM with circular coherence correction

c) TFM with phase coherence corection

d) TFM with sign coherence corection

Figure 30: TFM images with the phase coherence correction for the isotropic case

3.4.3 Finely grained material (0.48mm)

First, let us compare the multistatic response matrix and its singular values, as shown in Figure 2.5a and Figure 2.5b. Even with fine grains, the effect of structural noise is significant - the scattering pattern of the notch is now barely distinguishable and the division between the signal and noise subspaces of the singular values is more arbitrary. As demonstrated below, the same follows for imaging results.

3.4.3.1 SR Images

The images computed using different variants of the TR-MUSIC algorithm are shown in Figure 32. The SNR in the TFM image deteriorated, but the defect signature is still distinguishable. However, the TR-MUSIC at single, centre frequency performs very poorly, offering no information about the defect. Amplitude-based addition of the contribtion of different frequencies allows the peak to start forming, but the resolution is low and both SNR and CNR are far smaller than for the TFM image. The phase-coherent TR-MUSIC method provides excellent resolution, with the edge of the notch precisely located. The SNR is low, but the noise background is fairly constant, leading to high CNR.

The TFM images with phase coherence corrections are shown in Figure 33. Analogously to the isotropic case, the improvement in both SNR and CNR is impressive. PCF and SCF variants offer better vertical resolution, but the latter at a cost of sidelobes along the vertical direction. These results indicate that the phase coherence correction is a relatively simple enhancement to TFM, but allows for a significant improvement over both classical TFM and SR imaging.

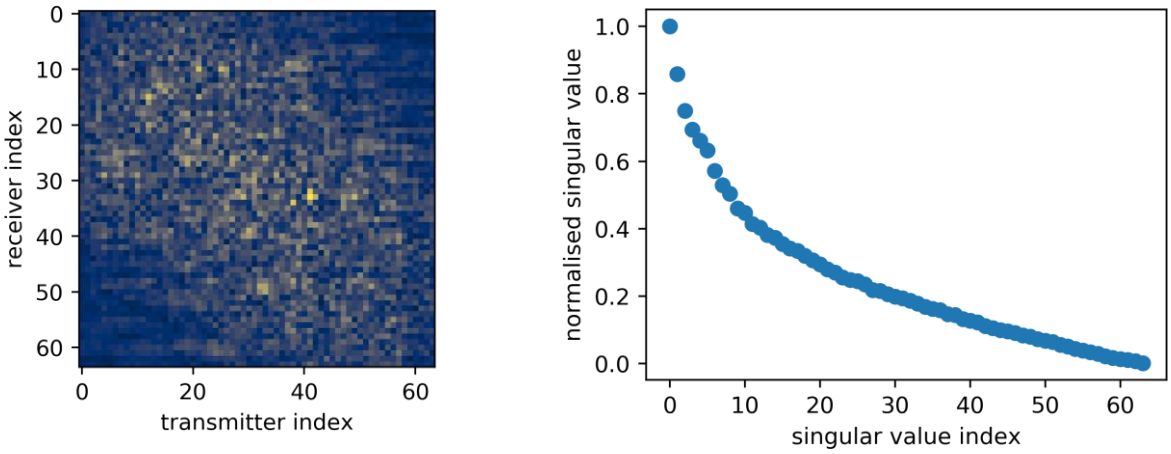

a) $|\mathbf{K}(\omega)|$

b) Singular values

Figure 31: The multistatic response matrix at the centre frequency of 2 MHz for the finely-grained model

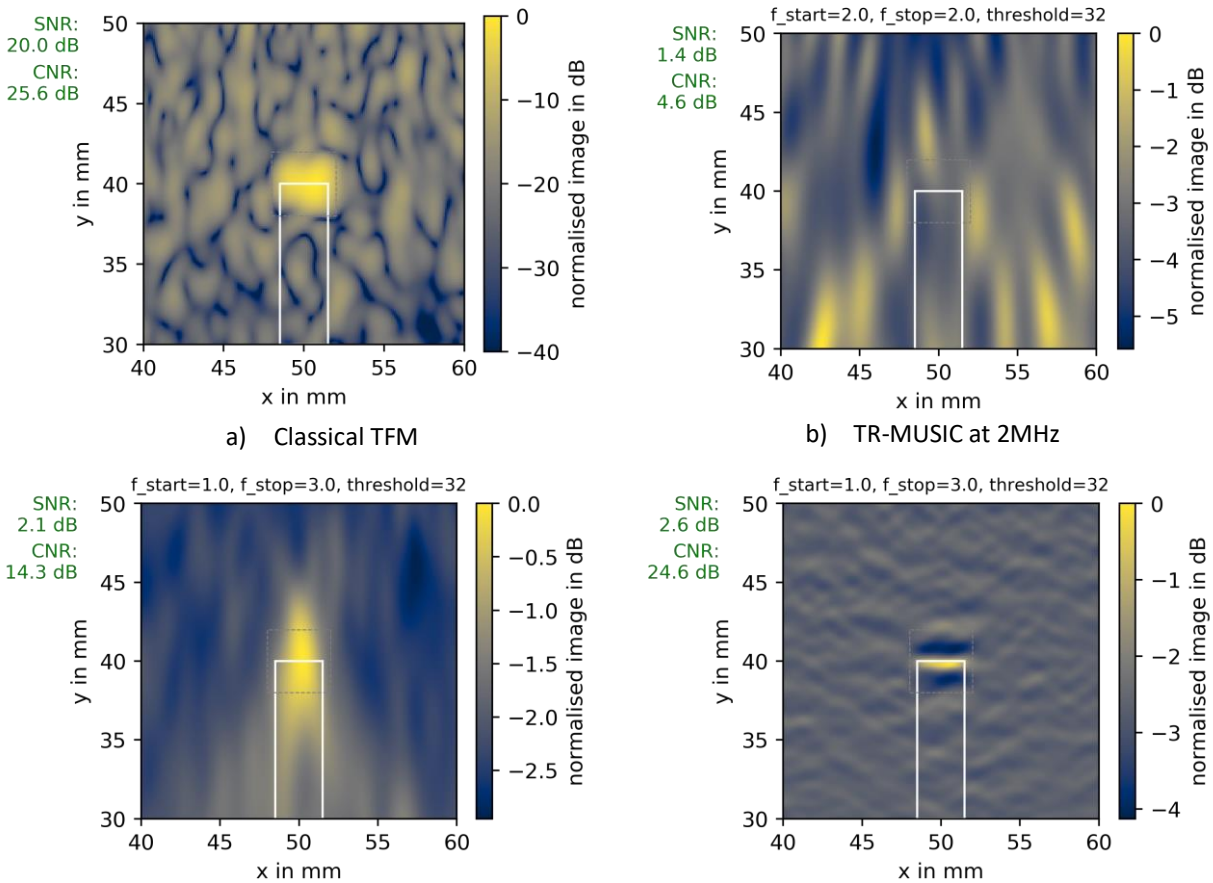

a) Classical TFM

b) TR-MUSIC at 2MHz

c) MF-TR-MUSIC between 1 and 3MHz

d) PC-MUSIC between 1 and 3MHz

Figure 32: SR images for the fine grain case

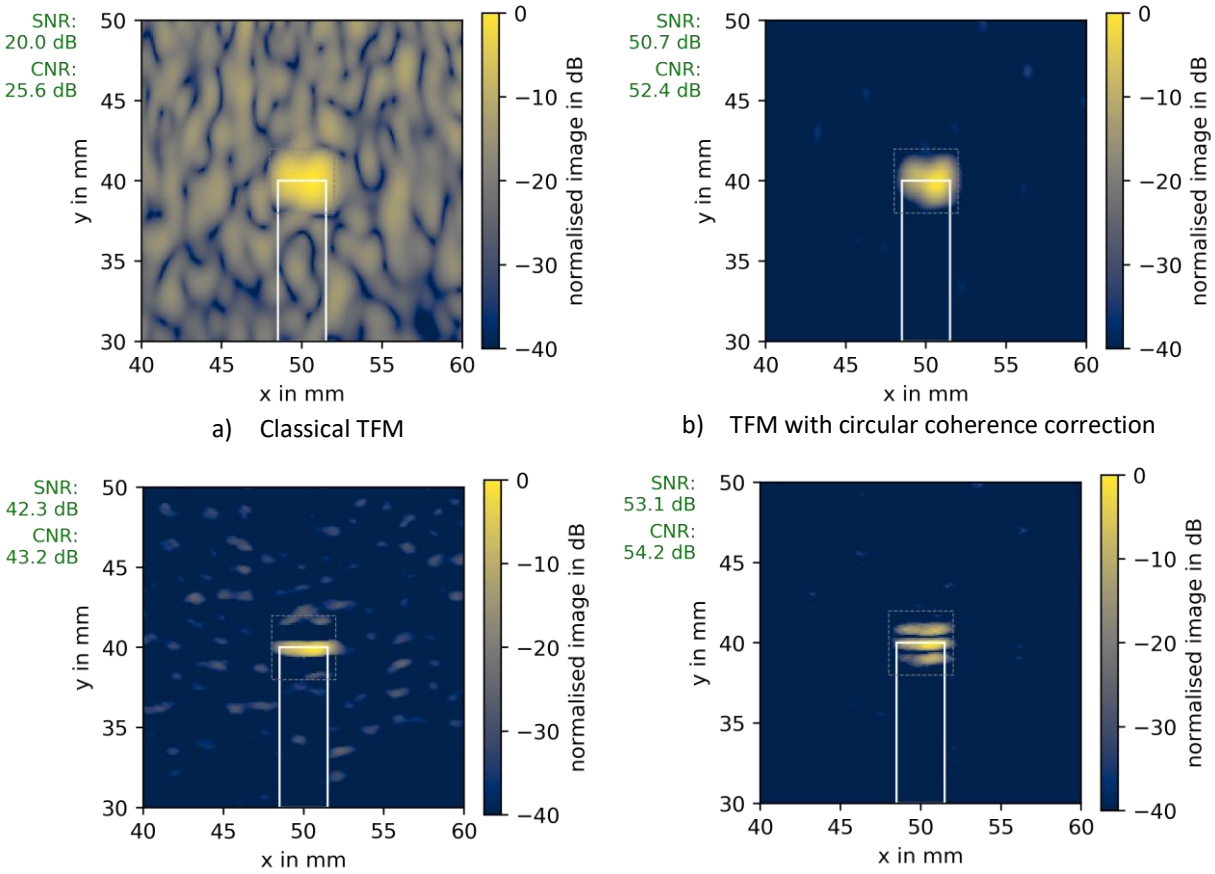

a) Classical TFM

b) TFM with circular coherence correction

c) TFM with phase coherence corection

d) TFM with sign coherence corection

Figure 33: TFM images with the phase coherence correction for the finely-grained case

Table 6: The comparison of SNR and CNR for the finely-grained model

test case/imaging method		TFM				TR-MUSIC		
		Classical	CCF	PCF	SCF	CF		PC
isotropic	SNR	20	50.7	42.3	53.1	n/a	2.1	2.6
	CNR	25.6	52.4	43.2	54.2	n/a	14.3	24.6

3.4.4 Coarsely-grained material (0.96mm)

SR images for the coarsely-grained model are shown in Figure 34. Following the observations form the preceding case, the TR-MUSIC image computed at the centre frequency is not shown. The multi-frequency variant indicates the location of the target, but the vertical resolution is very low and the image metrics not satisfactory. Two PC-MUSIC images are plotted, one computed over the 1-3 MHz band (Figure 34c) and the other at slightly lower frequencies, between 0.7 and 1.5 MHz (Figure 34d. Shifting to lower frequencies enabled the grain noise to be slightly reduced, leading to improved SNR and CNR. To further verify this, we plot the images computed using the lowest and the highest bands of the spectrum of **K** in Figure 35. Interestingly, the low frequency image looses the target information entirely, while the high frequency one amplifies the grain noise. It may be concluded that SR images need to be computed over a frequency band that contains most of the signal's energy.

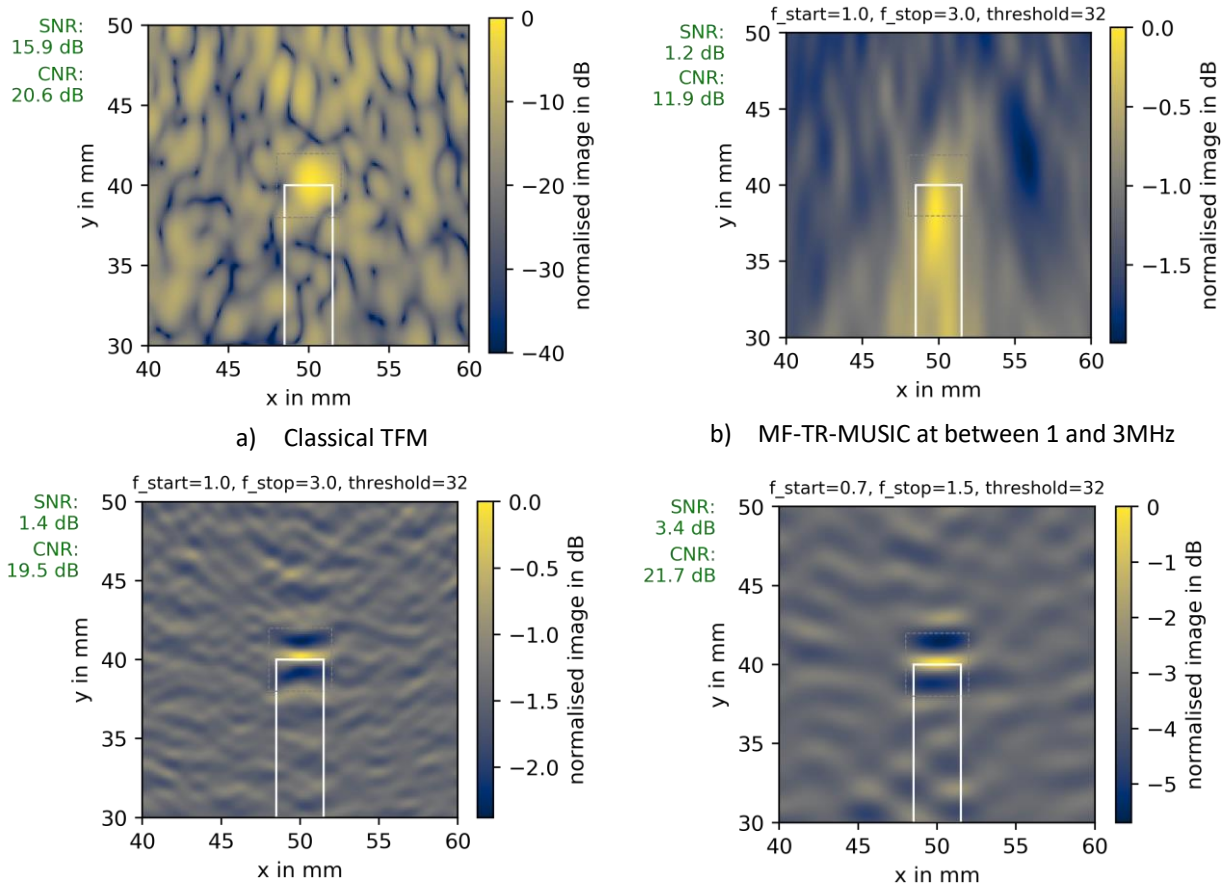

a) Classical TFM

b) MF-TR-MUSIC at between 1 and 3MHz

c) PC-MUSIC between 1 and 3MHz

d) PC-MUSIC between 0.7 and 1.5MHz

Figure 34: SR images for the coarsely-grained case

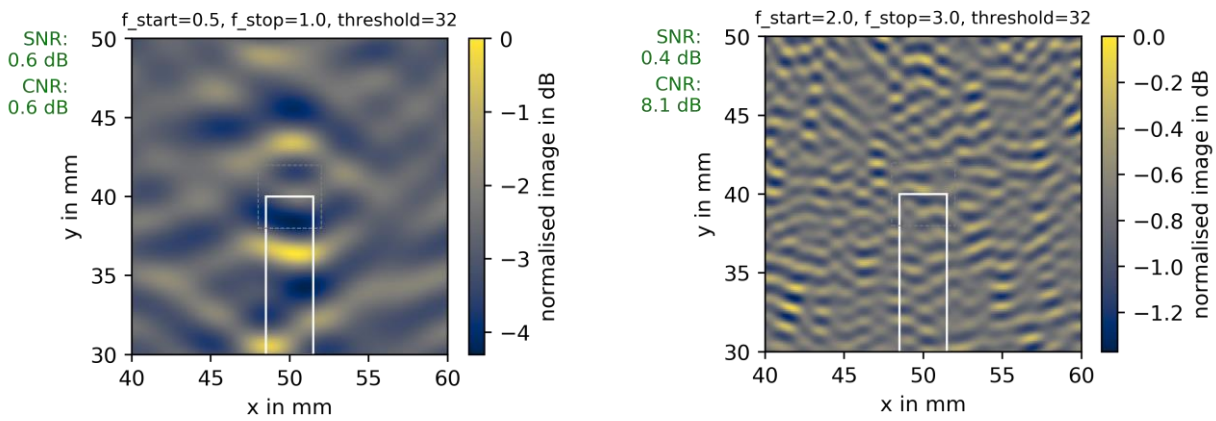

a) PC-MUSIC between 0.5 and 1MHz

b) PC-MUSIC at between 2 and 3MHz

Figure 35: SR images focused on the low and high frequencies for the coarsely-grained case

As a comparison, the TFM images are shown in Figure 36. Like in the finely-grained case, the improvement in both SNR and CNR is significant, typically above 20 dB. Moreover, PCF and SCF variants shown considerably improved resolution. The side lobes in the vertical direction are present again in the SCF image, but they do not seem to affect its legibility.

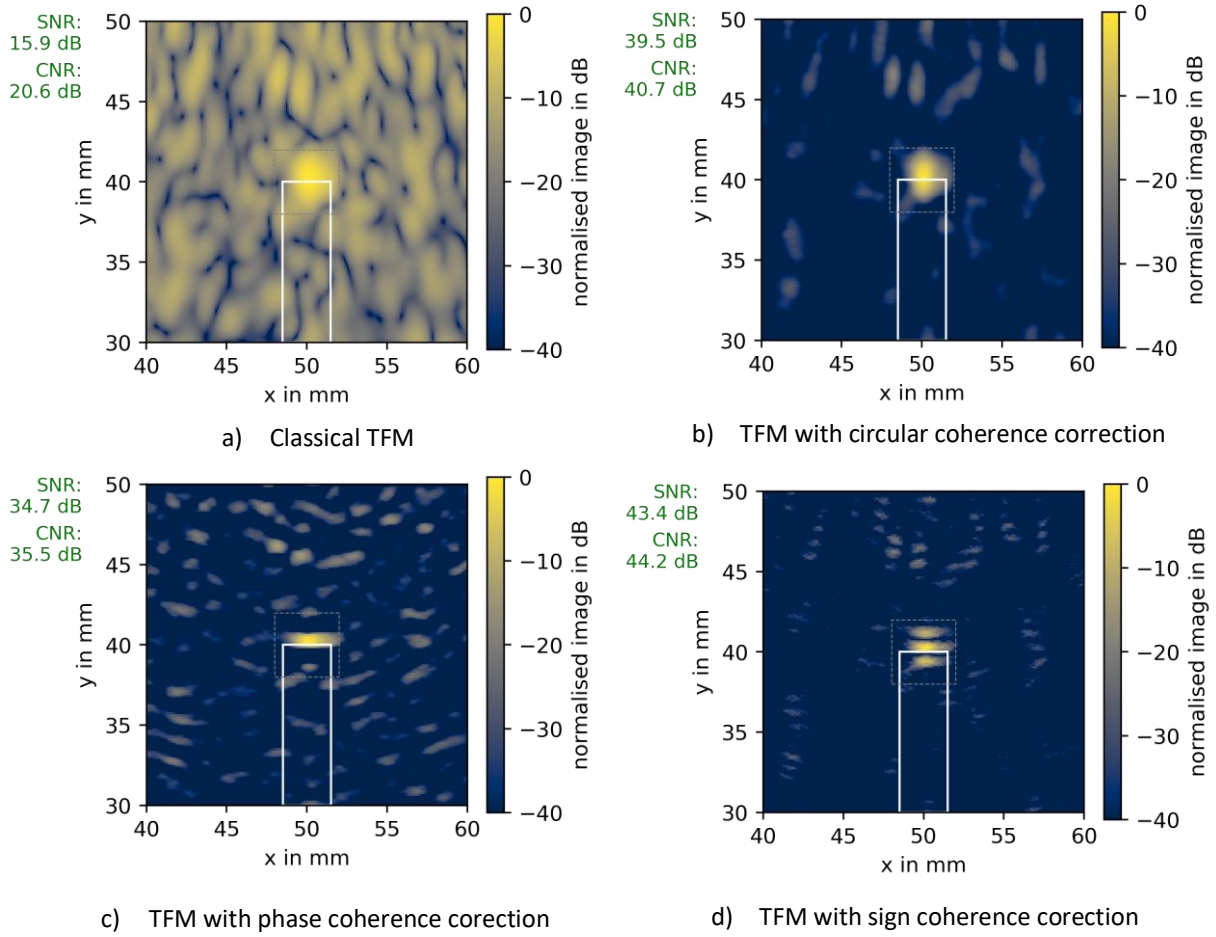

a) Classical TFM

b) TFM with circular coherence correction

c) TFM with phase coherence corection

d) TFM with sign coherence corection

Figure 36: TFM images with the phase coherence correction for the coarsely-grained case

Table 7: The comparison of SNR and CNR for the coarsely-grained model

test case/imaging method		TFM				TR-MUSIC		
		Classical	CCF	PCF	SCF	CF		PC
isotropic	SNR	15.9	39.5	34.7	43.4	n/a	1.2	3.4
	CNR	20.6	40.7	35.5	44.2	n/a/	11.9	21.7

3.4.5 Very coarsely-grained material (1.95mm)

The final variant of the model is composed of very coarse grains. It is expected that the signatures of the defect are entirely buried in backscattered signals. SR images for this case are shown in Figure 37. The images cannot be deemed legible and, surprisingly, the phase-coherent algorithm is unable to enhance the true scatterer fingerprint. Including lower frequencies, as in Figure 37c adds more sidelobes and increases the variance in the proportion of the image covered by grain noise.

© ADVISE consortium

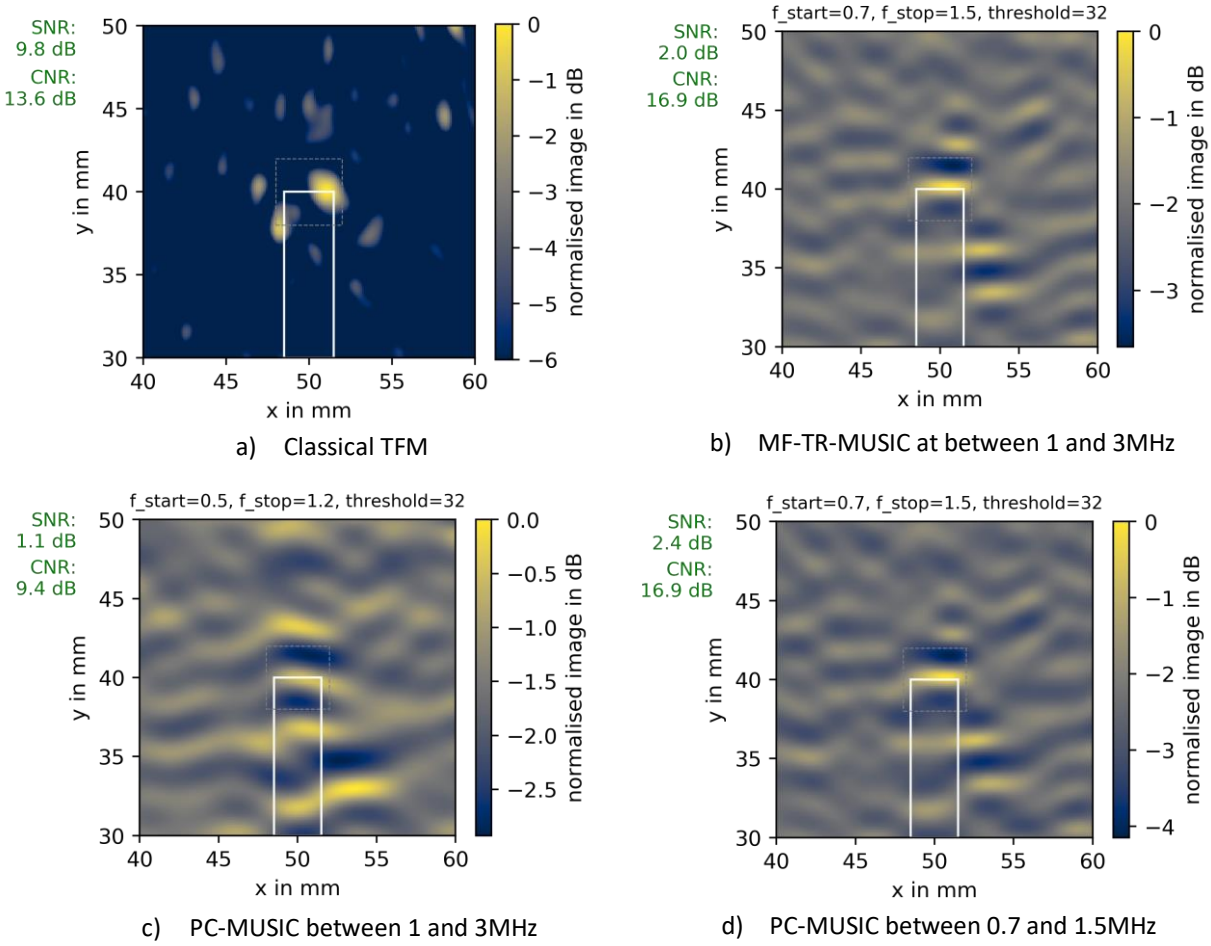

Figure 37: SR images for the very coarsely-grained case

The TFM images are shown in Figure 38. While the comparison metrics are quite high (> 20 dB), these correspond to a maximum value in the signal region. In this case, the images have been intentionally presented down to -6dB from the maximum to improve the legibility. The right corner of the notch is well represented, but the left one is weaker and shifted down slightly, indicating the contribution of beam deviation. Although these can be observed, in real world applications it is more likely that these features are mistaken for noise.

Table 8: The comparison of SNR and CNR for the very coarsely-grained model (the values below should be taken with care - they ofter correspond to 'single-pixel' maxima)

test case/imaging method		TFM				TR-MUSIC		
		Classical	CCF	PCF	SCF	CF		PC
isotropic	SNR	9.8	21.9	21.3	25.2	n/a	n/a	2.4
	CNR	13.6	22.8	24.6	25.7	n/a	n/a	16.9

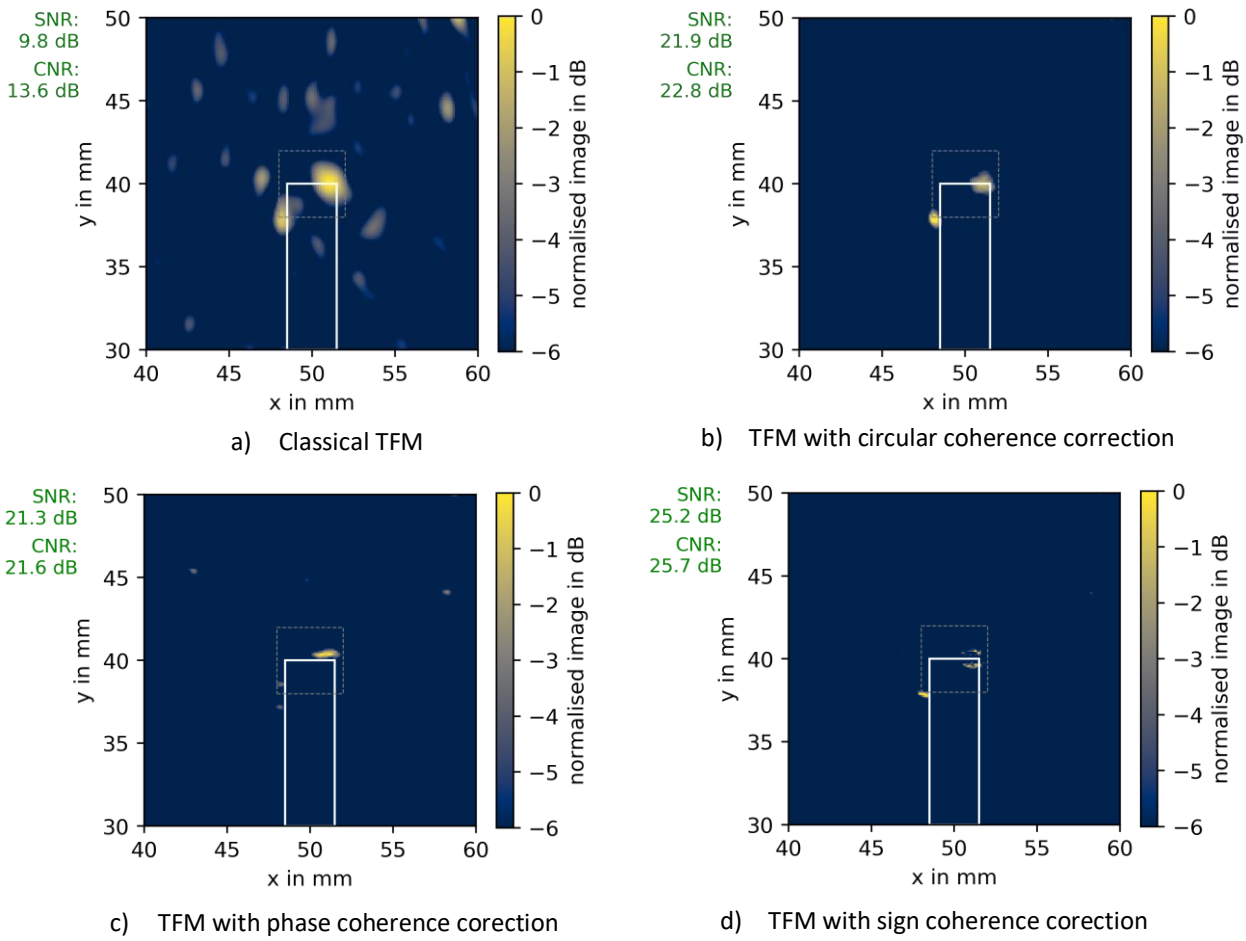

a) Classical TFM

b) TFM with circular coherence correction

c) TFM with phase coherence corection

d) TFM with sign coherence corection

Figure 38: TFM images with the phase coherence correction for the very coarsely-grained case

3.4.6 Summary

The simulated results demonstrated the strengths and weaknesses of super-resolution algorithms for coarsely-grained materials. We showed that using the phase-coherent variant of TR-MUSIC is essential for obtaining legible defect signatures. SR images often present relatively high CNR, but low SNR. The noise level is high but with small variance, hence true scatterers stand out clearly.

SR images were compared to classical TFM images and TFM images with phase coherence corrections (three variants). Overall, the corrected images improved both SNR and CNR significantly, often well over 20 dB, increasing the resolution at the same time. They were found to be more robust to structural noise and were found considerably clearer than the corresponding SR images. Moreover, the calculation of TFM images with phase coherence correction is considerably more straightforward. It does not require signal gating, choosing the frequency band or deciding the threshold for the number of singular vectors. All these are an indispensable part of SR image generation and often need to be addressed on a case-by-case basis.

Simulated examples confirmed that the classical TFM is relatively robust to noise and straightforward to compute. With phase coherence corrections, it seems to be the first choice for processing array data for coarsely grained materials.

3.5 Experimental TRL array results

In this section, we apply the methods discussed above to the TRL array data collected at KTU. The detailed description of the experimental setup is not presented here for brevity. The mock-up sample supplied by Framatome is made of Inconel with grain sizes described by a sum of two distributions, one averaging at 0.3

mm and the other at 2.4 mm. The sample has a series of flat bottom holes (FBH) of which three are used in this study. Figure 2a contains a schematic drawing of the sample. A 1 MHz 32-element TRL array with custom-made wedges is placed on the top surface.

The observations reported in the preceding section indicate that only the phase coherent variant of the SR algorithm may yield legible results. The best obtained SR images for the three defects are shown in Figure 39. Note that they were computed based on the approximate location of the defects read from TFM images.

Although the promise of applying SR algorithms to data affected by structural noise indicated focusing on lower frequencies, images computed over bandwidths lower than that in Figure 39 were of considerably lower quality. Here, while the defect signatures are clear, except for the FBH E (Figure 40, it is unlikely that these images can be reliably used in a practical setting. The required a priori knowledge of the defect location and the need of tuning the frequency bandwidth and the size of the signal subspace make the process rather tedious.

In Figs 40-42, we show the TFM images, both the classical and phase coherence-corrected variants for each FBH separately. The phase coherence correction dramatically reduces the grain noise in the images related to FBH 'C' and 'D', while amplifying the signatures of the FBH end. Note that the images are normalised with respect to the maximum value of an image in the 'signal' region. The backwall feature is very strong but can be easily distinguished from the scatterers of interest. If needed, several techniques for eliminating the backwall signature may be used, e.g. [11].

For FBH 'E', according to Figure 42, it is unlikely that reliable detection is possible. This may be partially attributed to the fact that it is the furthest defect from the array of all the three considered.

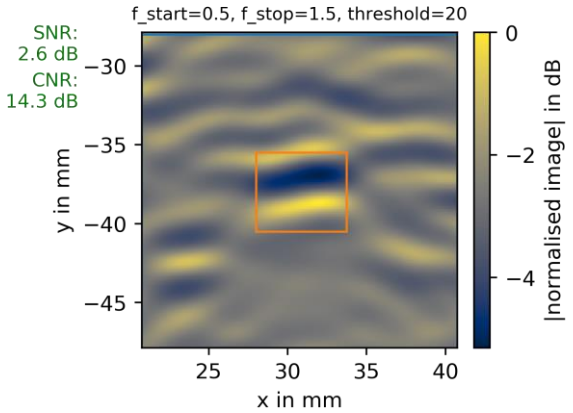

a) FBH C, 20 singular vectors, frequency bandwidth 0.5 – 1.5 MHz

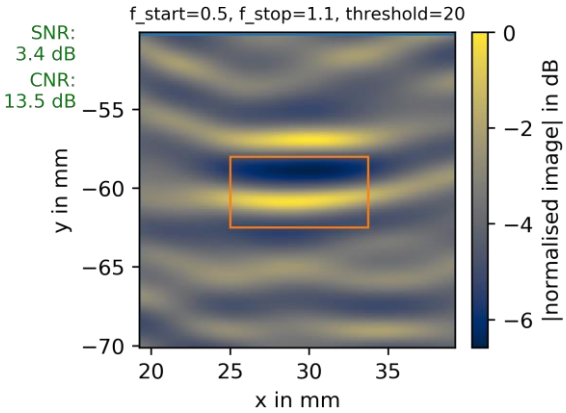

b) FBH D, 20 singular vectors, frequency bandwidth 0.5 – 1.1 MHz

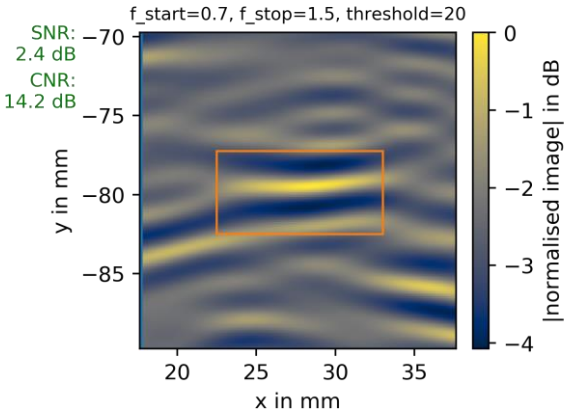

c) FBH E, 20 singular vectors, frequency bandwidth 0.7 – 1.5 MHz

Figure 39: PC-MUSIC images for the three flat bottom holes based on TRL array data

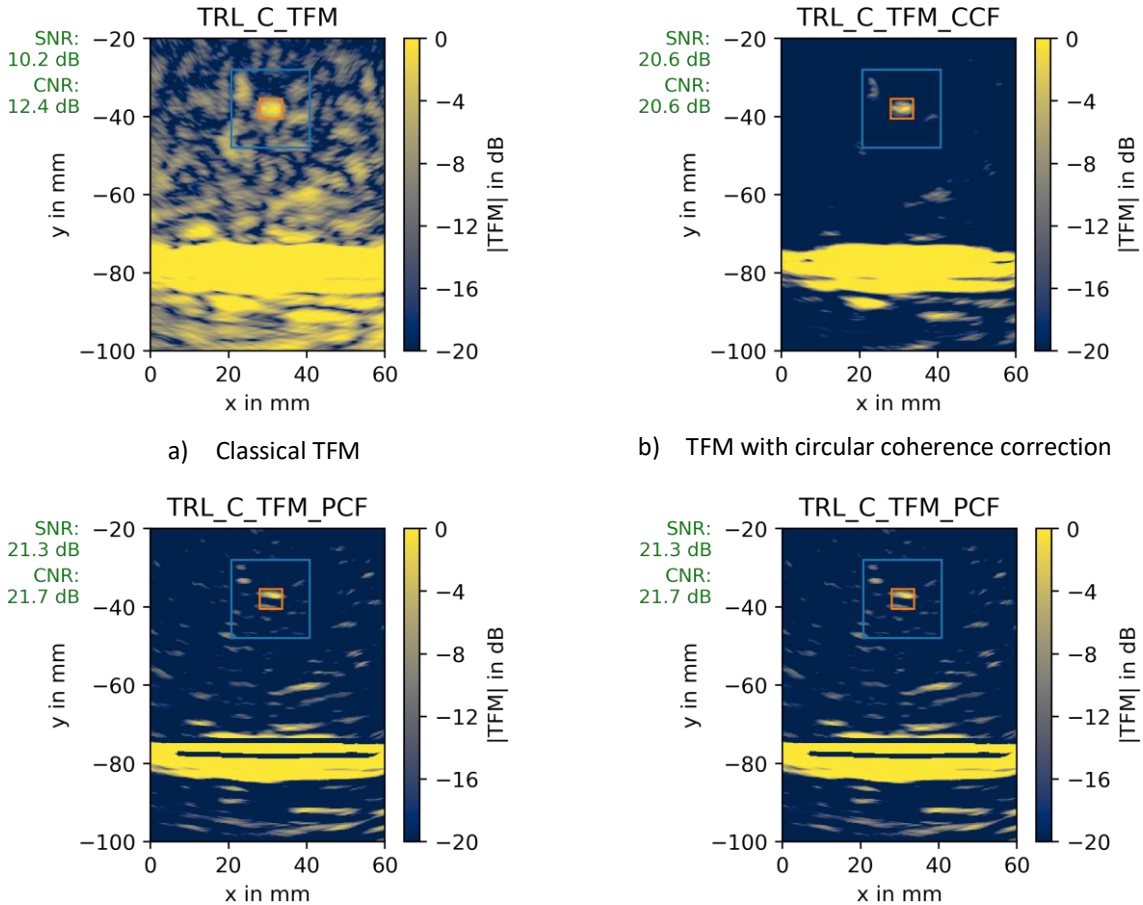

a) Classical TFM

b) TFM with circular coherence correction

c) TFM with phase coherence corection

d) TFM with sign coherence corection

Figure 40: TFM images with the phase coherence correction for the flat bottom hole `C', based on TRL array data

© ADVISE consortium

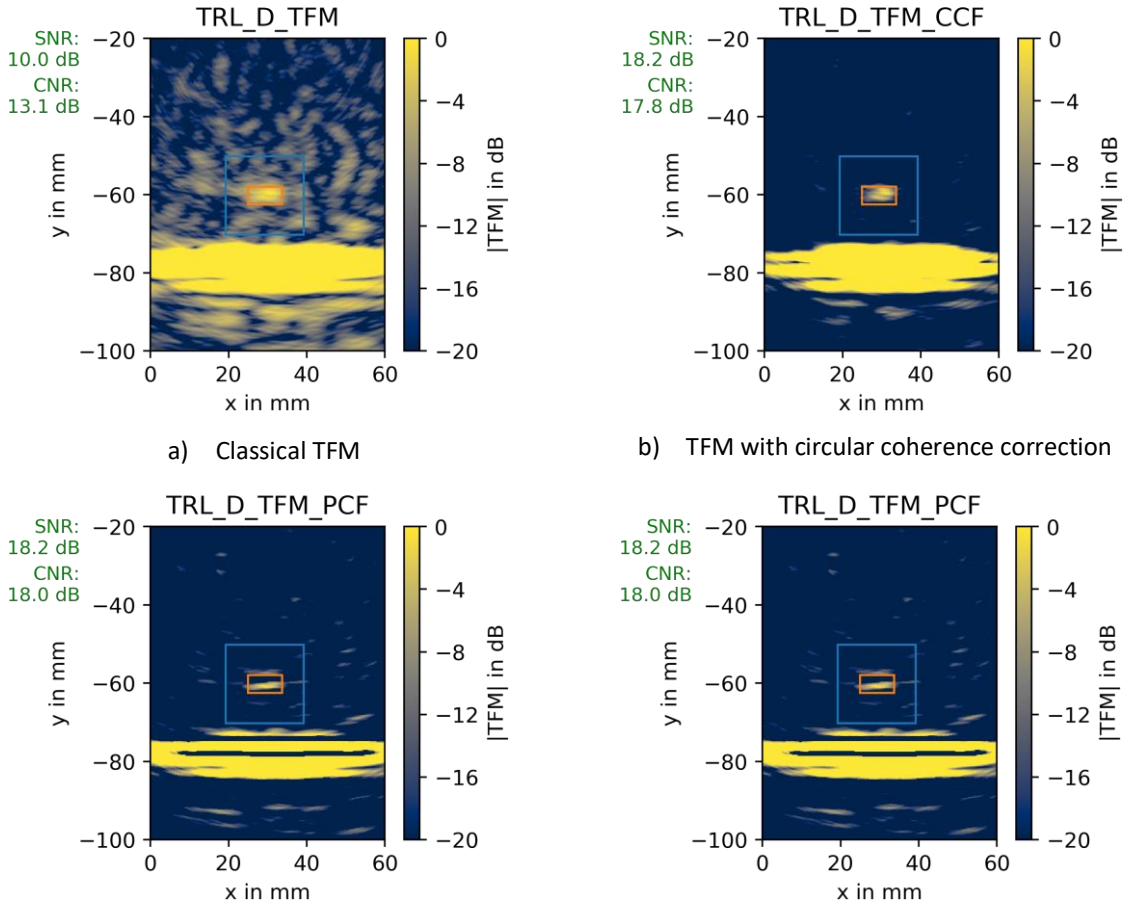

a) Classical TFM

b) TFM with circular coherence correction

c) TFM with phase coherence corection

d) TFM with sign coherence corection

Figure 41: TFM images with the phase coherence correction for the flat bottom hole `D', based on TRL array data

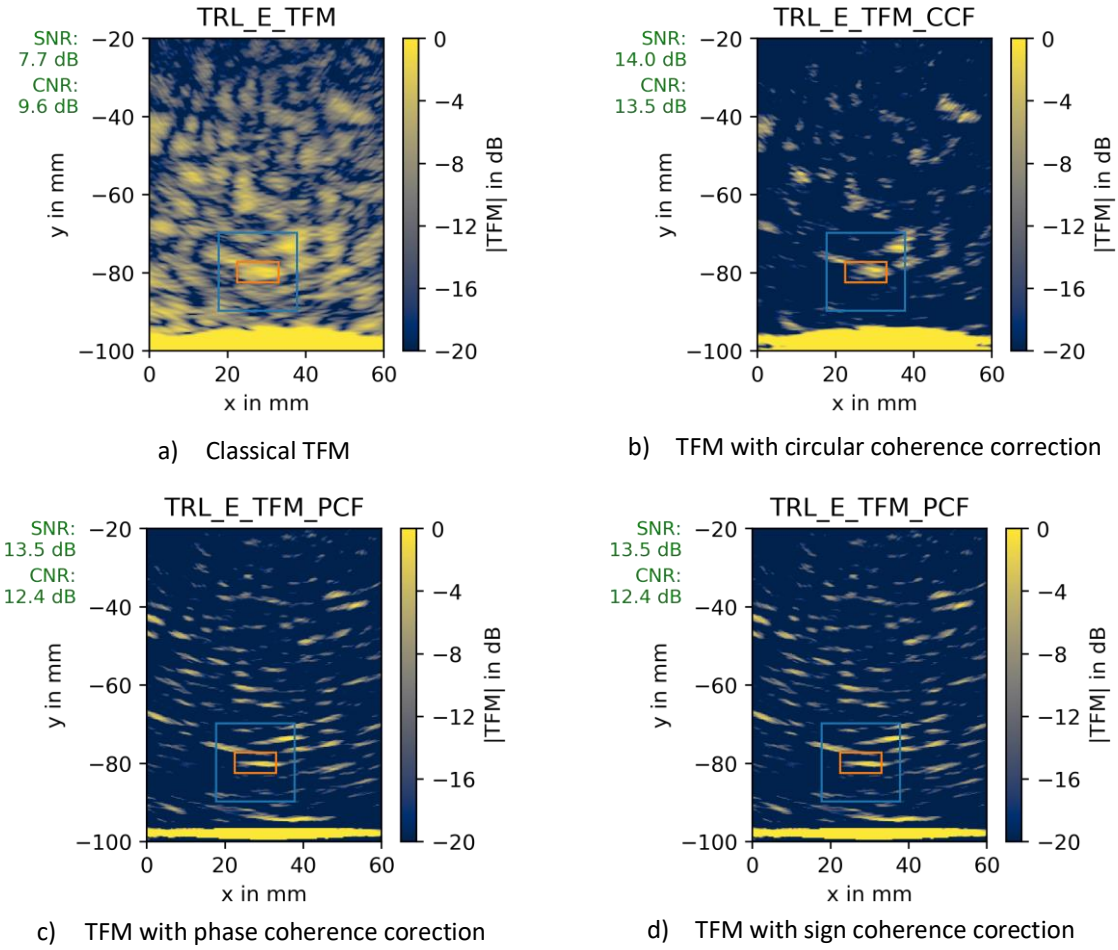

a) Classical TFM

b) TFM with circular coherence correction

c) TFM with phase coherence corection

d) TFM with sign coherence corection

Figure 42: TFM images with the phase coherence correction for the flat bottom hole `E', based on TRL array data

3.5.1 Summary

We showed that SR algorithms do not provide a reliable way to compute array images for coarsely grained materials. They are very sensitive to noise, and even the best variant, enhanced by phase coherence was not able to recover defect signatures from the noise level to a satisfactory degree. Applying phase coherence correction to TFM images was found to be more effective, more robust to noise and easier to compute.

© ADVISE consortium

4 Conclusions

1. The advantages of using TRL probes over arrays in pulse echo mode for inspection of heterogeneous materials have been demonstrated in this report. Despite that classical PE inspection provides better lateral resolution and amplitude at the focal point, overall TRL gives an increase in SNR, which is achieved by separation between transmission and reflection apertures leading to reduced the effective material volume generating backscatter noise.
2. On average TRL gives 3dB increase in SNR comparing to the SScan images obtained with sectorial scanning between 25° and 65° and by focusing at the depth of the corresponding defect at 2MHz. The results demonstrated a slight discrepancy between the positions of the echoes and the actual positions of the defects in sample D343-CND2. The positioning error increases while depth decreases, which can be related to the variation in phase velocity and heterogeneity of sample D343-CND2. The positioning errors have to be taken into the account, as the measurements demonstrated that for 0° incidence no error was observed, while at 45° it was quite significant.
3. Plane wave transmission experiments demonstrated that PWI increases SNR by 4dB on average in comparison to TFM, while the number of transmissions is reduced by a factor of 2. This is a well-known result in heterogeneous materials: diverging waves are more attenuated than plane waves due to the attenuation caused by cylindrical spreading, and, since diverging waves interact with a maximum number of heterogeneities, they tend to increase the scattering noise contribution. A plane wave interacts with fewer heterogeneities of the material because the illuminated region is limited by the array aperture, and thus the scattering noise contribution is reduced.
4. The measurements on the sample with FBH defects (RDIM3) demonstrated that SNR at the beam convergence point is higher for TRL-TFM than in pulse-echo TFM. The conventional pulse-echo measurement showed better performance detecting subsurface defects, as the TRL wedge was designed to converge at depths 40mm to 80mm. However, the SNR in case of pulse-echo TFM significantly decreased with the depth of material, while TRL-TFM showed increasing SNR and overall decrease of structural noise at locations outside beam convergence area. It is important to note that sample RDIM3 had FBH defects which were inspected from the top, which gives reflection magnitude -32dB in respect to backwall at 1MHz.
5. The flat bottomed hole measurements also revealed that TRL-TFM enables to slightly enlarge reconstruction depth. The hole located at depth of 80mm was succesfully detected using TRL-TFM, while classical pulse-echo TFM failed. TRL-TFM experiment demonstrated more flexibility compared to classical inspection methods. For example, using 0° incidence TRL wedges with matrix arrays it is possible to change the beam convergence depth dynamically by adjusting delay times of array elements. On the other hand, both linear and matrix arrays can be used with 0° incidence TRL wedges to steer the beam in frontal direction, achieving different incidence angles. As a result, one wedge could be used instead of a set of wedges for longitudinal wave focusing at particular depth and incidence angle.
6. The Super Resolution methods have been evaluated on structures possesing different grain sizes with the intention to evaluate usuefulness of such methods for inspection of coarse-grained materials. It was found that using the phase-coherent variant of TR-MUSIC is essential for obtaining legible defect signatures. SR images often present relatively high CNR, but low SNR. The noise level is high but with small variance, hence true scatterers stand out clearly. It was found that SR algorithms do not provide a reliable way to compute array images for coarsely grained materials, since even the phase-coherent variant did not perform well on the experimental datasets. SR algorithms are very sensitive to noise, and even the best variant, enhanced by phase coherence was not able to recover defect signatures from the noise level to a satisfactory degree.
7. SR images were compared to classical TFM images and TFM images with phase coherence corrections (three variants). Overall, the corrected images improved both SNR and CNR significantly, often well over 20 dB, increasing the resolution at the same time. They were found to be more robust to structural noise and were found considerably clearer than the corresponding SR images. Applying phase coherence correction to TFM images was found to be more effective, more robust to noise and easier to compute.

 © ADVISE consortium

5 References

1. A.J. Devaney. “Time reversal imaging of obscured targets from multistatic data”. In:IEEE Transactions on Antennas and Propagation53.5 (May 2005). Conference Name: IEEE Transactions onAntennas and Propagation, pp. 1600–1610.issn: 1558-2221.doi:10.1109/TAP.2005.846723.
2. Jorge Camacho and Carlos Fritsch. “Phase coherence imaging of grained materials”. In:IEEE Transac-tions on Ultrasonics, Ferroelectrics, and Frequency Control58.5 (May 2011). Conference Name: IEEETransactions on Ultrasonics, Ferroelectrics, and Frequency Control, pp. 1006–1015.issn: 1525-8955.doi:10.1109/TUFFC.2011.1901.
3. Joshua B. Elliott, Michael J. S. Lowe, Peter Huthwaite, Richard Phillips, and David J. Duxbury.“Sizing Subwavelength Defects With Ultrasonic Imagery: An Assessment of Super-Resolution Imagingon Simulated Rough Defects”. In:IEEE Transactions on Ultrasonics, Ferroelectrics, and FrequencyControl66.10 (Oct. 2019). Conference Name: IEEE Transactions on Ultrasonics, Ferroelectrics, andFrequency Control, pp. 1634–1648.issn: 1525-8955.doi:10.1109/TUFFC.2019.2925974.
4. Chengguang Fan, Mihai Caleap, Mengchun Pan, and Bruce W. Drinkwater. “A comparison betweenultrasonic array beamforming and super resolution imaging algorithms for non-destructive evaluation”.In:Ultrasonics54.7 (Sept. 1, 2014), pp. 1842–1850.issn: 0041-624X.doi:10.1016/j.ultras.2013.12.012. (Visited on 05/01/2020).
5. Songming Hou, Kai Huang, Knut Solna, and Hongkai Zhao. “A phase and space coherent directimaging method”. In:The Journal of the Acoustical Society of America125.1 (Jan. 1, 2009). Publisher:Acoustical Society of America, pp. 227–238.issn: 0001-4966.doi:10.1121/1.3035835.
6. Endrias G. Asgedom, Leiv-J. Gelius, Andreas Austeng, Sverre Holm, and Martin Tygel. “Time-reversalmultiple signal classification in case of noise: A phase-coherent approach”. In:The Journal of theAcoustical Society of America130.4 (Oct. 1, 2011). Publisher: Acoustical Society of America, pp. 2024–2034.issn: 0001-4966.doi:10.1121/1.3626526.
7. Yassin Labyed and Lianjie Huang. “Super-resolution ultrasound imaging using a phase-coherent MU-SIC method with compensation for the phase response of transducer elements”. In:IEEE Transac-tions on Ultrasonics, Ferroelectrics, and Frequency Control60.6 (June 2013). Conference Name: IEEETransactions on Ultrasonics, Ferroelectrics, and Frequency Control, pp. 1048–1060.issn: 1525-8955.doi:10.1109/TUFFC.2013.2669.
8. Chengguang Fan, Lei Yang, and Yong Zhao. “Ultrasonic multi-frequency time-reversal-based imagingof extended targets”. In:NDT & E International(Apr. 20, 2020), p. 102276.issn: 0963-8695.doi:10.1016/j.ndteint.2020.102276.
9. J. Camacho, M. Parrilla, and C. Fritsch. “Phase Coherence Imaging”. In:IEEE Transactions on Ultra-sonics, Ferroelectrics, and Frequency Control56.5 (May 2009). Conference Name: IEEE Transactionson Ultrasonics, Ferroelectrics, and Frequency Control, pp. 958–974.issn: 1525-8955.doi:10.1109/TUFFC.2009.1128.
10. Anton Van Pamel, Colin R. Brett, and Michael J.S. Lowe. “A methodology for evaluating detectionperformance of ultrasonic array imaging algorithms for coarse-grained materials”. In:IEEE Transac-tions on Ultrasonics, Ferroelectrics, and Frequency Control61.12 (Dec. 2014), pp. 2042–2053.issn:0885-3010.doi:10.1109/TUFFC.2014.006429.
11. C. Zhang, P. Huthwaite, and M. Lowe. “The Application of the Factorization Method to the Subsur-face Imaging of Surface-Breaking Cracks”. In:IEEE Transactions on Ultrasonics, Ferroelectrics, andFrequency Control65.3 (2018), pp. 497–512.